RSC Advances

PAPER

View Article Online
View Journal | View Issue

Cite this: *RSC Adv.*, 2022, **12**, 14665

Synthesis and characterization of novel dicarbohydrazide derivatives with electrochemical and theoretical approaches as potential corrosion inhibitors for N80 steel in a 3.5% NaCl solution†

Y. M. Abdallah, *[a] Ola. A. El-Gammal,[b] Hany M. Abd El-Lateef[cd] and K. Shalabi *[b]

Two novel ethanoanthracene-11,12-dicarbohydrazide derivatives N'^{11},N'^{12}-bis((*Z*)-4-hydroxybenzylidene)-9,10-dihydro-9,10-ethanoanthracene-11,12-dicarbohydrazide (H_2HEH) and N'^{11},N'^{12}-bis((*Z*)-4-methoxybenzylidene)-9,10-dihydro-9,10-ethanoanthracene-11,12-dicarbohydrazide (H_2MEH) were synthesized and characterized by FT-IR spectroscopy, electronic spectra, and NMR spectroscopy. These two derivatives as novel anticorrosion inhibitors for N80 steel in a 3.5% NaCl solution were studied using electrochemical techniques including potentiodynamic polarization (PP), electrochemical impedance spectroscopy (EIS), and electrochemical frequency modulation (EFM). Corrosion parameters and adsorption isotherms were determined from current–potential diagrams (*i.e.*, Tafel slopes). The impact of temperature and inhibitor concentration on the corrosion performance was studied using the PP method. The PP results suggested mixed-type inhibitors. The inhibition prohibition increased and decreased when the dose was increased and the temperature was increased, respectively. The adsorption of the hydrazides on the N80 exterior followed the Langmuir isotherm. The maximum inhibition proficiency for H_2MEH and H_2HEH were 93.3% and 92.2%, respectively, at 1×10^{-4} M. Moreover, the investigated surface was studied with the synthesized compounds through X-ray photoelectron spectroscopy (XPS) to confirm the construction of an adsorbed shielding barrier. An evident association was established between the corrosion inhibition proficiency and theoretical variables acquired using the density functional theory (DFT) method and Monte Carlo (MC) simulations. The experimental data were in good agreement with the theoretical results.

Received 17th March 2022
Accepted 2nd May 2022

DOI: 10.1039/d2ra01751b

rsc.li/rsc-advances

1. Introduction

Energy becomes increasingly important as industries, population, and living standards rise. As a result, governments must model and forecast their energy consumption. The variables used in the literature for estimating energy consumption are grouped according to the three primary elements of sustainability: social, economic, and environmental issues. Advancements in corrosion science research are important for the protection of alloys and metals and in the discipline of economics. Particularly, the inhibition of N80 steel corrosion is of interest since this type of steel has been thoroughly applied as the construction material in various industries including chemical, electrochemical, medicinal, nuclear power, petroleum, control, and food manufacturing. The corrosion of steel in oil pipelines is a multifaceted progression that represents significant difficulties. This is because of the confined corrosion, which results from the aggression of certain media. The corrosion is typically minimized by the addition of inhibitors in small concentrations. The most profitable inhibitors are the organic components that include heteroatoms such as sulfur, nitrogen and oxygen.[1–3]

Moreover, various studies have recommended the use of heteroatom-containing organic components with functional groups such as –OH, $–NH_2$, $–OCH_3$, –COOH, $–SO_3H$ and benzene rings. These compounds have been found to be potential inhibitors since they can react with a metal or alloy to produce a protective film coating on a tested surface.[4–7]

Quantum chemical computations have been extensively exploited to survey the mechanisms of corrosion and to explain the experimental data.[6] They have been used to elucidate vague chemical results and are found suitable for the understanding

[a]*Department of Dental Biomaterials, Faculty of Oral and Dental Medicine, Delta University for Science and Technology, Gamasa, Egypt. E-mail: dr.ymostafa8@gmail.com; Yasser.Mostafa@deltauniv.edu.eg*

[b]*Chemistry Department, Faculty of Science, Mansoura University, P.O. Box 70, Mansoura, Egypt. E-mail: dr-kamal@mans.edu.eg*

[c]*Department of Chemistry, College of Science, King Faisal University, Al-Ahsa 31982, Saudi Arabia. E-mail: hmahmed@kfu.edu.sa*

[d]*Department of Chemistry, Faculty of Science, Sohag University, Sohag 82524, Egypt*

† Electronic supplementary information (ESI) available. See https://doi.org/10.1039/d2ra01751b

of corrosion mechanisms in examined particles on a metal exterior.[7] The variables in the preparation and electronics of inhibitor components could be explained by the concepts of theoretical estimation using the computerized approaches of quantum chemistry.[8]

An appropriate approach to corrosion protection on metals and composites is the addition of organic derivatives to corrosive media.[9,10]

Furthermore, organic inhibitors that include electron-donating heteroatoms such as –N, –O, –S and π-electrons associated with heterocyclic bonds are strong metals and composite inhibitors in corrosive solutions.[11–17] An issue with the utilization of corrosion inhibitors is the adsorption of an inhibitor on the external surfaces of metals and composites from a solution. Consequently, the examinations of organic compounds on corroded carbon steel in acidic corrosive media showed many indentations; thus, they are mostly insufficient.[18–20]

Carbon steel has been examined using different corrosive media, including: hydrazones,[21] anti-tuberculosis drugs,[22] Stachys byzantina extracts,[23] interfacial assembled mesoporous polydopamine nanoparticles,[24] Zn(II)-metal–organic networks using lemon verbena leaf extract,[25] 2-aminopyridine derivatives,[26] and benzodiazepine derivatives.[27]

The environmental significance of hydrazide derivatives is due to their biocompatibility. Hydrazides have been explored for their corrosion mitigating properties.[28] In this study, the effectiveness of hydrazide derivatives as corrosion inhibitors were on the basis of the fact that they have a wide spectrum of medicinal chemistry use due to their biological features such as analgesic and anti-inflammatory effects, which have been well documented in numerous studies.[29,30] Isonicotinic acid hydrazide is unquestionably effective in tuberculosis treatment, whereas fatty acid hydrazides have been applied as fabric processing agents.[31]

In acidic and neutral environments, hydrazide derivatives have been approved as corrosion inhibitors. The corrosion inhibitors, including salicylic acid, anthranilic acid, and benzoic acid hydrazides with AOH, ANH_2, and AH as characteristic substituents, have been investigated. The potentiodynamic polarization (PP) technique revealed that they showed a mixed-type inhibitory activity for mild steel corrosion.[32] Kumari *et al.*[33] investigated the aromatic hydrazide derivative of 2-(3,4,5-trimethoxybenzylidene) hydrazinecarbothioamide as a mixed-type inhibitor with prohibition efficacy that increased in both cathodic and anodic directions. Ferrocene carboxaldehyde propanoylhydrazone and ferrocene carboxaldehyde furoylhydrazone that were derived from hydrazides,[34] aromatic sulfonohydrazides, hydroxy phenyl hydrazide,[35] *N*-[4-(diethylamino) benzylidine]-3-{[8-(trifluoromethyl) quinolin-4-yl]thio}propano hydrazide[36] and 2-(2-hydrazinyl-1,6-dihydro-6-oxopyrimidin-4-yl)acetohydrazide,[37] have been tested as potential corrosion inhibitors. Here, dicarbohydrazide compounds were chosen as inhibitors since it was clear from the literature that hydrazides efficiently decreased corrosion.

Hence, in this study, we report the synthesis of some novel dicarbohydrazide derivatives and evaluate them as effective corrosion inhibitors for N80 carbon steel in neutral corrosive media (*i.e.*, 3.5% NaCl solution).

We investigated the synthesis and characterization of two novel hydrazides derivatives including ethanoanthracene-11,12-dicarbohydrazide derivatives N'^{11},N'^{12}-bis((*Z*)-4-hydroxybenzylidene)-9,10-dihydro-9,10-ethanoanthracene-11,12-dicarbohydrazide (**H_2HEH**) and N'^{11},N'^{12}-bis((*Z*)-4-methoxybenzylidene)-9,10-dihydro-9,10-ethanoanthracene-11,12-dicarbohydrazide (**H_2MEH**). They were tested as corrosion inhibitors of N80 steel in a 3.5% NaCl solution. Characterization methods used include potentiodynamic polarization (PP), electrochemical frequency modulation, EFM, and electrochemical impedance spectroscopy (EIS). In addition, X-ray photoelectron spectroscopy (XPS) was employed to verify the creation of an adsorbed protective film, discuss the mechanism of corrosion, and match the experimental data with the theoretical outcomes achieved from the density functional theory (DFT) calculations and Monte Carlo (MC) simulations.

2. Materials and methods

2.1. Synthesis of the inhibitors

The hydrazides, namely **H_2HEH** and **H_2MEH** (Scheme 1), were synthesized by the dropwise addition of an ethanolic solution of *p*-methoxybezaldehyde or *p*-hydroxybenzaldehyde to an ethanolic solution of hydrazide, with 9,10-dihydro-9,10-ethanoanthracene-11,12-dicarbohydrazide in a 2 : 1 molar ratio.[38] The reaction mixture was refluxed for 4 h until a white precipitate was obtained. The precipitate was filtered, then rinsed with ethanol, dried and finally, preserved in a vacuum desiccator with anhydrous $CaCl_2$ (m.p. = 260 °C and 280 °C for **H_2HEH** and **H_2MEH**, respectively). Our novel hydrazides were synthesized using ultrapure reagents acquired from the Aldrich-sigma company.

2.1.1. H_2HEH. $C_{32}H_{26}O_4N_4$ (530.58) m.p. 252–253 °C, beige; yield: 80%; Anal. calcd%: C 72.44; H 4.94; N 12.06; found: C 71.13; H 5. 25; N 11.85; FTIR (cm^{-1}): 3238 $\nu(N^1H)$; 3340 $\nu(N^4H)$; 3328 $\nu(N^2H)$; 1670 $\nu(C{=}O)_{free}$; 1708 $\nu(C{=}O)_{bonded}$; 1565, 1246 and 637 ν(amide I–III); 1322 δ(C–H); 916 δ(N–H); 1608 $\nu(C{=}C)_{phenyl}$; 1045 ν (N–N); UV-vis in DMF (33 222, 25 062); ^{1}H NMR (δ, ppm): 3.24 (dd, J = 3.6 Hz, 2H), 4.11, 4.24 (m, 2H), OCH_3 3.48 (s, 3H), 3.65 (s, 3H), 7.31 (d, J = 9.0 Hz, 4H), 7.20–7.65 (m, 12H), 8.40 (s, 2H), OH 11.25 (s, 2H); NH 11.25 (s, 1H); azomethine H δ = 8. 75 ppm (s, 2H).

2.1.2. H_2MEH. $C_{34}H_{30}O_4N_4$ (558.64) m.p. 264–265 °C, white; yield: 84%; Anal. calcd%: C 73.10; H 5.41; N 10.02; Found: C 74.03; H 5. 35; N 9.85; FTIR (cm^{-1}): 3234 $\nu(N^1H)$; 3330 $\nu(N^4H)$; 3321 $\nu(N^2H)$; 1662 $\nu(C{=}O)_{free}$; 1703 $\nu(C{=}O)_{bonded}$; 1575, 1266 and 625 ν(amide I–III); 1322 δ(C–H); 918 δ(*N*–H); 1605 $\nu(C{=}C)_{phenyl}$; 1040 ν (N–N); UV-vis in DMF (33 003, 25 308); ^{1}H NMR (δ, ppm): 3.24 (dd, J = 3.6 Hz, 2H), 3.40–3.53 (m, 2H), 3.75 (s, 3H), 3.91 (s, 3H), 6.85 (d, J = 9.0 Hz, 4H), 7.19–7.66 (m, 12H), 8.41, 8.47 (s, 2H, azomethine), NH 11.44 (s, 1H).

2.2. Materials and reagents

An N80 steel specimen with a composition (weight%) of C (0.31%), S (0.008%), P (0.01%), Si (0.19%), Mn (0.92%), Cr

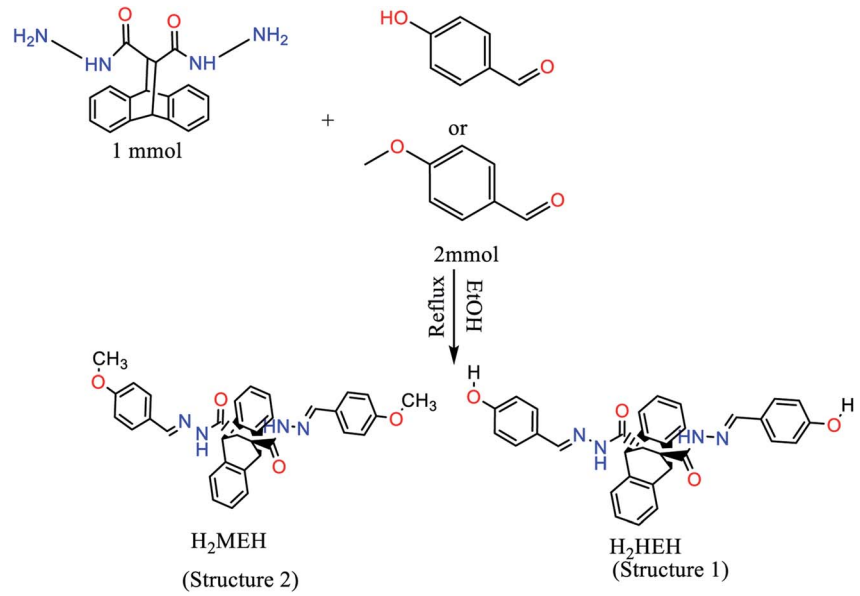

Scheme 1 Synthesized hydrazides of H_2HEH and H_2MEH scheme.

Table 1 Molecular compositions of the examined inhibitors and their molecular weight

Compounds	Name	Structure	Molecular weight & chemical formula
H_2HEH	N'^{11},N'^{12}-Bis((*Z*)-4-hydroxybenzylidene)-9,10-dihydro-9,10-ethanoanthracene-11,12-dicarbohydrazide	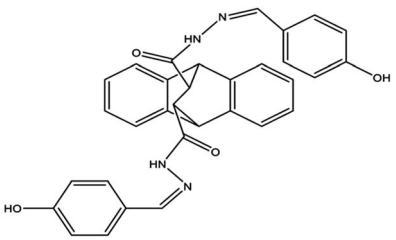	$C_{32}H_{26}O_4N_4$, 530.58
H_2MEH	N'^{11},N'^{12}-Bis((*Z*)-4-methoxybenzylidene)-9,10-dihydro-9,10-ethanoanthracene-11,12-dicarbohydrazide	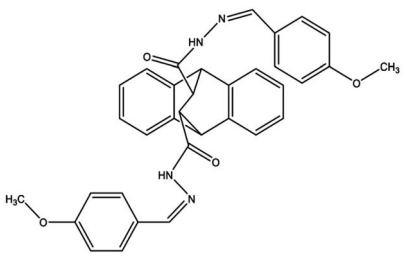	$C_{34}H_{30}O_4N_4$, 558.64

(0.20%) and Fe (remaining) was used to make a working electrode, which had a rectangular design having a surface area of 1 cm^2. The specimen was scraped by applying various grades (up to 1000 grade) of emery papers. It was degreased within propanone solution, purified with double distilled water, and dehydrated with soft tissues. The experiments were conducted in 3.5% NaCl solution before and after adding altered doses of the hydrazide derivatives. The concentrations of the inhibitors used were between 1×10^{-6} M and 1×10^{-4} M. Per investigation (Table 1), a new solution that had been freshly prepared was employed.

2.3. Electrochemical measurements

Electrochemical trials were performed utilizing a standard three-electrode cell (S4), which included an N80 steel sample as the working electrode and enclosed in an epoxy resin of polytetrafluoroethylene. A saturated calomel electrode (SCE) and a Pt sheet (1 cm^2) were used as the reference and auxiliary electrodes, respectively. An SCE was associated with a Luggin capillary where the crown of this capillary was located near the tested electrode to diminish the IR drop. The reaction chamber was opened to the atmosphere and measurements were performed at 25 ± 1 °C. All potential standards were noted *vs.* SCE.

Before each trial, the N80 steel surface was grazed with various grades of emery papers, degreased with a basic solution (15 g Na_2CO_3 + 15 g Na_3PO_4 per liter)[39] scrubbed in double distilled water, and finally desiccated.

Tafel polarization diagrams (PP) were achieved by modifying the potential values between 1100 to −200 mV SCE at a scan rate of 1 mV s^{-1}. The Stern–Geary approach[40] was employed for determining the corrosion current and was executed through the inferences of anodic and cathodic Tafel shapes of the charge transfer in the two directions. This was done to give a value that provides (log i_{corr}) and equivalent corrosion potential (E_{corr}) for the blank solution and each dose of the tested compounds. The i_{corr} was applied to calculate the inhibition potency (η%) and surface covering (θ) by the equation below:

$$\eta\% = \theta \times 100 = \left(1 - \frac{i_{corr(inh)}}{i_{corr(free)}}\right) \times 100 \quad (1)$$

where "$i_{corr(free)}$ and $i_{corr(inh)}$ are the current densities in the absence and presence of the inhibitor", respectively.

Impedance measurements with an amplitude of 5 mV were carried out in the frequency range of 10 kHz to 0.1 Hz (peak-to-peak through ac signals at OCP).

The impedances were examined and constructed from the corresponding circuits (Fig. 5). The calculated variables from Nyquist plots were the charge transfer resistance (R_{ct}) and the capacity of the double layer (C_{dl}). The inhibition prohibition (η%) and the surface coverage (θ) data were achieved utilizing the EIS technique and the values were determined according to the equation below:

$$\eta\% = \theta \times 100 = \left(1 - \left[\frac{R_{ct}^{\circ}}{R_{ct}}\right]\right) \times 100 \quad (2)$$

where "R_{ct} and R_{ct}° are the charge transfer resistances in the absence and presence of the inhibitor", accordingly.

At frequencies of 2 and 5 Hz, EFM measurements were performed. Because the base frequency was 0.1 Hz, a wave was replicated in 1 second. The current responses, which were assigned to harmonious and intermodulation current peaks, were included in the intermodulation spectra. The i_{corr}, Tafel slopes (β_c and β_a), and causality factors were estimated using stronger peaks (CF-2 and CF-3).[40]

Each electrochemical test was repeated 3 times to emphasize data duplicability.

The electrode potential was stabilized for 30 min prior to each trial. All trials were performed at 25 ± 1 °C. All evaluations were conducted on a Gamry Instrument Potentiostat/Galvanostat/ZRA. This comprised a Gamry framework system that was predicated on the ESA 400. Gamry techniques contained a DC105 for DC corrosion calculations, EIS 300 for EIS, and EFM 140 for EFM calculations. The instrument was connected to a computer for data gathering. The Echem analyst 6.25 software was applied for designing and fitting our data.

2.4. XPS analysis

A high-resolution XPS model K-ALPHA (Thermo Fisher Scientific, USA) with a monochromatic X-ray Al K-alpha radiation was used to study the treated N80 carbon steel (inhibited) in 3.5% NaCl with 1×10^{-4} M of **H_2MEH** at 25 ± 1 °C.

2.5. DFT calculations and MC simulations

Theoretical surveys were achieved using the DMol^3 module for DFT estimations. The MC simulations were carried out using an adsorption locator module *via* the Materials Studio software V.7.0 from Accelrys Inc. USA. In the DFT computations, the forms of the hydrazide derivatives were optimized by applying a B3LYP functional with a DNP base set and COSMO solvation controls. These inputs were described in our earlier work, where numerous quantum parameters for hydrazide derivatives were calculated.[41,42]

For MC simulations, the adsorption locator disclosed the proper adsorption formations of the protonated forms of the hydrazide derivatives by Monte Carlo investigations on Fe (1 1 0) exterior.[43] This was to estimate the inhibition efficiency of the hydrazide derivatives. The adsorption of the hydrazide derivatives, water particles, and Fe (1 1 0) exterior was achieved in a simulation box (32.27 Å × 32.27 Å × 50.18 Å) within a periodic boundary tuning. Forcite classical simulation engine was applied to improve the particle energy of the hydrazides.[44] The specifics of the relevant computations have been reported recently.[41,44]

3. Results and discussion

3.1. Characterization of the synthesized hydrazides derivatives

3.1.1. FT-IR spectral characterization. Fig. S1(A) and (B)† show the most significant IR bands of the hydrazides (in KBr discs) under investigation. The IR spectrum of **H_2HEH** (structure 1) (A) exhibited bands at 3453, 3315, 3117 and 1613 cm^{-1} that are attributed to a ν(OH)$_{ring}$, ν(NH), ν(C=C) $_{phenyl}$ and ν(C=N), respectively. The strongest band was at 1658 cm^{-1}, which was assigned to a ν(C=O) mode. The ν(C=N)$_{azome}$ was revealed at 1572 cm^{-1}. Finally, the band at 1043 cm^{-1} was most likely from a to ν(N–N) mode.[45] On the other hand, the spectrum (B) of **H_2MEH** (structure 2) shows bands of medium intensity at 3321 and 1613 cm^{-1} assignable to ν(NH) and ν(C=C)$_{phenyl}$, respectively.[46] The bands appearing as a doublet band at 1662 and 1625 cm^{-1} due to ν(C=O) suggested the presence of the compound in *syn* and *anti*-conforms. This assumption is affirmed from the ^{1}H NMR spectrum of this hydrazide (S2) as the signals of all hydrogens were doubled. Additionally, this was further affirmed by the molecular modeling of the title hydrazide, where the two isomers consumed similar binding energies (4043.32, 4043.48 kcal mol^{-1} for *anti* and *syn* isomers, respectively). The bands noted at 1542 and 1353 cm^{-1} are assigned to the imine group, ν(C=N)$_{azome}$ and ν(OCH_3) vibrational modes while that at 1043 cm^{-1} refers to the ν(N–N) mode.[47] In both hydrazides, the bands due to amide I–III are noted at (1565, 1246 and 637 cm^{-1}) and (1536, 1259 and 643 cm^{-1}) **H_2MEH** and **H_2HEH**, respectively.[48]

3.1.2. NMR spectral characterization. A glance at the H^1-NMR spectra in d_6-DMSO of both hydrazides indicated the possibility of isomerism as all signals as the protons are duplicated. In the ^{1}H NMR, the spectrum of **H_2HEH** (S2)

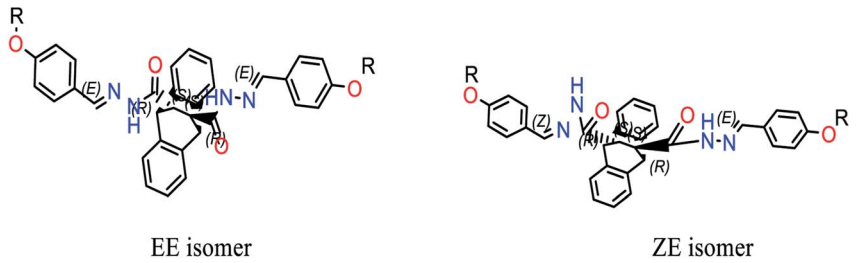

Scheme 2 Possible isomers of hydrazide (R = OCH_3; H).

exhibits signals at 11.66, 11.20 and 9.77 ppm assigned to the protons of phenolic OH, NH and azomethine (H–C═N), respectively. The multiplets at δ_H (ppm) {(6.99–7.04); (7.06–7.16), (7.18–7.34)} and (7.50–7.95), are due to protons of condensed and free aromatic rings of the hydrazide, respectively. Again, the protons of CH groups (CH13, CH14) (structures 1 and 2) appeared at δ_H 3.10; 3.46 (brs, 2H) and (CH15–CH19) at 4.51; 4.82 ppm (brs, 2H). On the other hand, the spectrum of **H_2MEH** in d_6-DMSO (S2) showed signals at 11.73, 11.20 and (9.16, 8.23 ppm) referring to the protons of NH and azomethine groups of *syn* and *anti*-isomers (Scheme 2). These signals disappeared upon adding D_2O. The signals due to the protons of the condensed and free aromatic rings of the hydrazide moiety are duplicated and revealed the presence of 18 protons, which were observed as multiplets at δ_H (ppm): {(7.01–7.16); (7.17–7.38), (7.49–7.51)} and (7.54–7.98), respectively. The protons of CH groups (CH13, CH14) (structures 1 and 2) appear at δ_H 3.32; 3.34 (brs, 2H) and (CH15–CH19) at 4.54; 4.88 ppm (brs, 2H), respectively. The configuration of the only two stereogenic centers C15 and C19 occurred as 15S and 19S, respectively, as a result of the appearance of the two broad singlets for H15 and H19 instead of the two doublets. The signals observed at δ_H 1.03–1.08 ppm are assignable to the protons of the OCH_3 group of the *syn* and *anti*-isomers.

(S3) shows the C^{13}NMR spectrum of **H_2MEH** in d_6-DMSO that supported the existence of the investigated hydrazide in tautomeric forms, as all signals are duplicated, revealing the existence of 34 carbon atoms, including two methylene groups at 38.60–40.33, four aliphatic methine groups at 44.90–47.41, four aliphatic methine groups at 45.3 and 46.6, two amidic carbon atoms (C═O) at 171.60,170.60, two azomethine (C═N) groups at 169.1, 167.87 and eight aromatic methine groups from 123.20 to 143.34 ppm, respectively.

3.1.3. Electronic spectra. The electronic spectra of **H_2HEH** and **H_2MEH** in DMF are provided in Fig. 1(A) and (B), respectively. They exhibited bands at 33 003 and 33 222 cm^{-1}, respectively, equivalent to the $\pi \rightarrow \pi^*$ transitions of the benzene rings in the two hydrazides. The bands that appeared as shoulders at 23 154, 21 270 and 19 047 cm^{-1} corresponded to $\pi \rightarrow \pi^*$ and $n \rightarrow \pi^*$ transitions. These are characteristics of the carbonyl and azomethine groups.[48]

3.2. Potentiodynamic polarization curves (PP)

Fig. 2a and b show the change in E_{OCP} *vs.* time for the inhibited and uninhibited N80 steel in 3.5% NaCl solutions through 30 min. As shown in Fig. 2a and b, the N80 steel in the uninhibited and inhibited systems reach a steady state after dipping for ≈900 s and the values of E_{OCP} exhibit a small modification (<0.001 V *vs.* SCE). For the inhibited samples with hydrazide derivatives, the values of E_{OCP} altered by less than 85 mV compared with the uninhibited samples for the period of the immersion designating that hydrazide derivatives operate as mixed-type inhibitors. The values of E_{OCP} slightly diminished with an immersion period up to ≈900 s. The unstable period could be known as the dynamic route of desorption and adsorption of the hydrazide derivatives at the interface of N80 steel/NaCl. After an exposure period ≈900s, the E_{OCP} values inclined to a steady-state, demonstrating that the adsorption

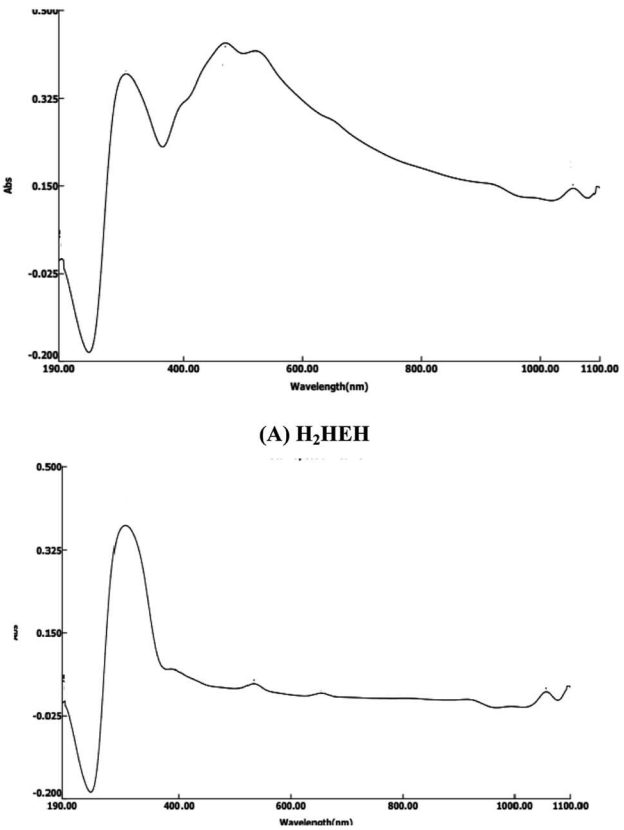

Fig. 1 UV-vis. Spectra of (A) H_2HEH and (B) H_2MEH.

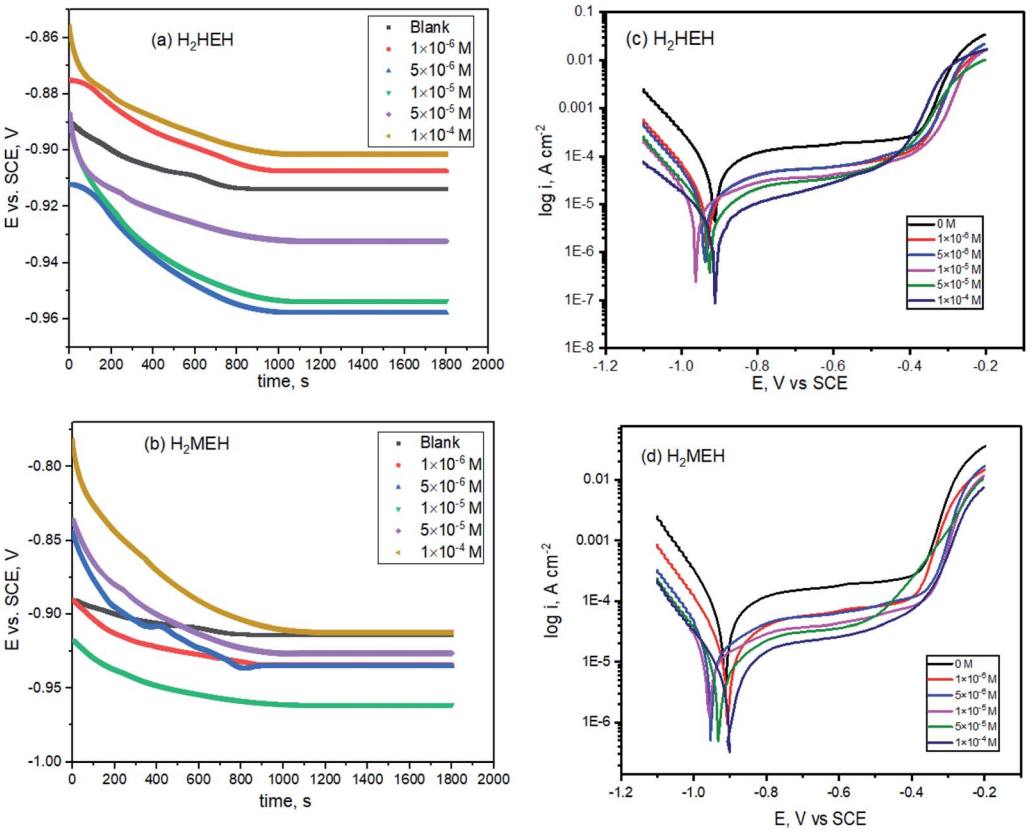

Fig. 2 Open circuit diagrams (a, b) and Tafel plots (c, d) for the corrosion of N80 steel in 3.5% NaCl solution in the lack and existence of diverse concentrations of the synthesized hydrazides.

Table 2 The electrochemical variables premeditated through the Tafel polarization method for the corrosion protection of N80 steel in the 3.5% NaCl medium without and with changed doses of the synthesized hydrazides at 25 ± 1 °C

Comp	Conc, M	$-E_{corr}$, mV	i_{corr}, μA cm^{-2}	β_a, mV dec^{-1}	β_c, mV dec^{-1}	C.R. mmy^{-1}	θ	η%
Blank	0.00	915	113.0 ± 5.65	1512	152	51.46	—	—
H_2HEH	1×10^{-6}	906	33.1 ± 2.31	999	142	15.12	0.707	70.7
	5×10^{-6}	954	30.4 ± 3.04	1026	139	13.87	0.731	73.1
	1×10^{-5}	958	21.0 ± 1.95	1042	138	9.61	0.814	81.4
	5×10^{-5}	931	15.4 ± 1.50	844	142	7.04	0.864	86.4
	1×10^{-4}	902	8.8 ± 0.08	613	150	4.02	0.922	92.2
H_2MEH	1×10^{-6}	933	30.1 ± 2.65	1025	135	13.74	0.734	73.4
	5×10^{-6}	939	27.0 ± 2.70	883	133	12.32	0.761	76.1
	1×10^{-5}	962	18.4 ± 1.20	956	127	8.39	0.837	83.7
	5×10^{-5}	928	14.0 ± 0.96	757	144	6.41	0.876	87.6
	1×10^{-4}	911	7.6 ± 0.07	524	182	3.45	0.933	93.3

and desorption of hydrazide's derivatives had touched a stable equilibrium.

Tafel curves are generally accepted to ensure suitable data on the kinetics of electrochemical corrosion variables. The presence of different concentrations of the prepared hydrazides changed each anodic plot and cathodic plot, as shown in Fig. 2c and d. These diminished the corrosion current density values, thereby creating a notable lowering in the corrosion rate values.

The anodic and cathodic current responses were reduced in the presence of compound I, as shown in Fig. 2. This influenced the expansions with the increase in the concentrations of **H_2HEH** and **H_2MEH**. The addition of **H_2HEH** and **H_2MEH** lowered the anodic dissolution of N80 specimens and delayed the cathodic oxygen reduction processes. The cathodic reaction in neutral solution (3.5% NaCl) consists of the reduction of oxygen into OH^- ions:

This performance was assigned to the adsorption of the **H_2HEH** and **H_2MEH** inhibitors on the active spots of the studied N80 steel sample.

The corrosion kinetic variables, including the corrosion potential (E_{corr}), anodic Tafel slope (β_a), cathodic Tafel slope (β_c) and corrosion current density (i_{corr}) were acquired from the PP

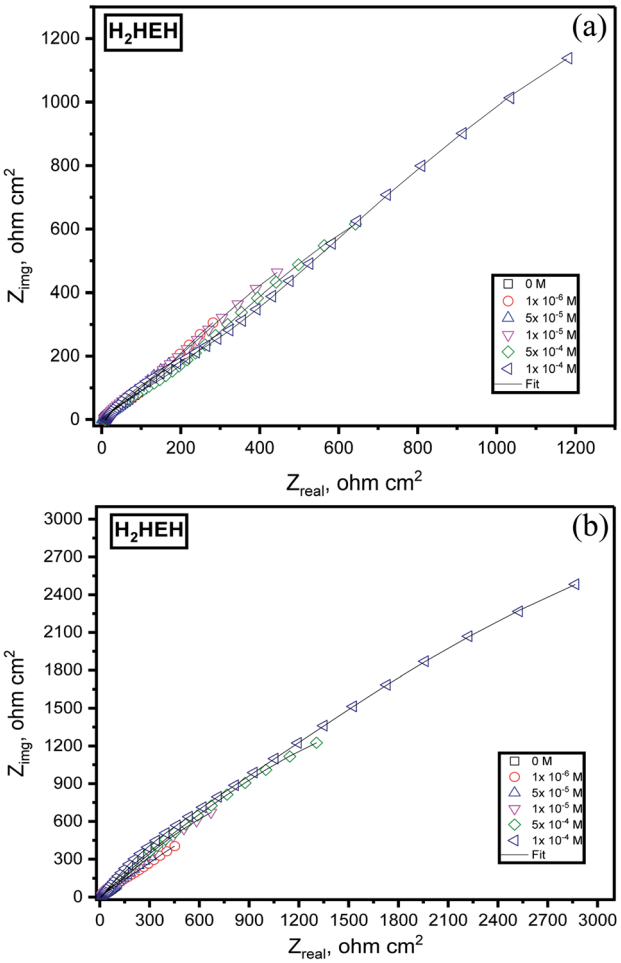

Fig. 3 Nyquist plots for the corrosion of N80 steel in 3.5% NaCl solution without and with various diverse synthesized hydrazides (a) H_2HEH and (b) H_2MEH.

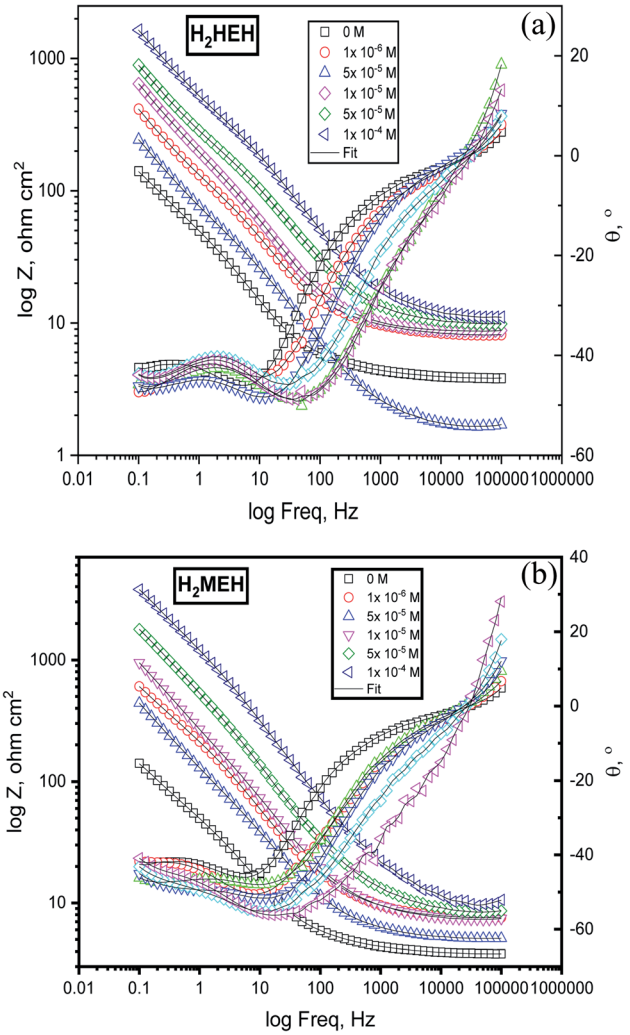

Fig. 4 Bode diagrams for the corrosion of N80 steel in 3.5% NaCl solution before and after adding altered doses of the synthesized hydrazides (a) H_2HEH and (b) H_2MEH.

figures and the data indicated in Table 2. The inhibition proficiency (η%) was considered by eqn (1).[49]

In the presence of **H_2HEH** and **H_2MEH**, the corrosion rate reduced, as exhibited in Fig. 2. The compounds also inhibit the cathodic hydrogen evolution and anodic metal dissolution reactions.[50–52] The changes in the values of β_a and β_c in the attendance of the compounds suggested the occurrence of the anodic metal dissolution and cathodic oxygen reduction processes. In the cathodic reaction, the inhibitor molecules were chemically adsorbed and retarded the O_2 reduction, while in the anodic reaction, the inhibitor molecules were physically adsorbed and hindered the dissolution of N80 metal. Furthermore, the high value of the anodic Tafel slope (β_a) is attributed to the oxide layer (passive layer) as a result of the oxygen existence in the solution that is more stabilized by the existence of inhibitors.[53] The reactions were enhanced by the increase in the concentration of the compounds. A shift in the values of E_{corr} at about 62 mV implied that the **H_2HEH** and **H_2MEH** compounds acted as mixed-type inhibitors.[54] The values of i_{corr} decreased from 113.0 to 7.6 mA cm^{-2} with the increase in the concentration of the compound. The inhibition efficacy was augmented to 93.3% owing to the adsorption of the inhibitors, which hindered the active sites on the N80 steel exterior. Additionally, the surface area that was accessible for Cl^- ions was reduced.[55]

3.3. EIS measurements

EIS extents were used to examine the components of the inhibition effect and the kinetics of the corrosion reactions. The surface characteristics, N80 steel kinetics and mechanical properties were obtained from the impedance plots. Fig. 3 was delineated from the Nyquist diagrams for the N80 steel in 3.5% NaCl in the presence and absence of diverse concentrations of (a) **H_2HEH** and (b) **H_2MEH**. Fig. 4 delineated from the Bode diagrams of the N80 steel in 3.5% NaCl with and without different concentrations of (a) **H_2HEH** and (b) **H_2MEH** acquired at the OCP.

The Nyquist diagrams were examined to be single capacitive loops suited with a one-time constant (*i.e.*, that seemed to be a single capacitive loop).[56] The capacitive loop at the high-

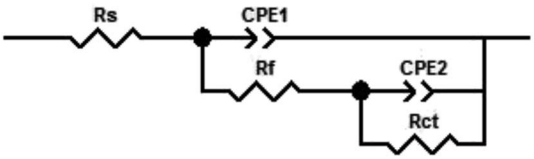

Fig. 5 Electrical corresponding circuit applied to fit the impedance results.

frequency area is assigned to the corrosion product/inhibitor film, and the capacitive loop at the middle-frequency area is assigned to the charge transfer reaction at the electrode/solution interface.[57] The size of the capacitive loop was found to rise with concentrations of the **H_2HEH** and **H_2MEH**. This was ascribed to the enlargement in the surface that was covered by the examined inhibitors on the N80 steel sample exterior.[58] To elucidate the frequency-independent phase change within the used alternating potential and current response, a constant phase element (CPE) was replaced by a double layer capacitance (C_{dl}). Additionally, phase angle *vs.* log frequency in Bode diagrams presenting two-phase crests are associated with the relaxation process of the electrical double layer capacitor and adsorbed **H_2HEH** and **H_2MEH**.[59] Furthermore, an incessant increase in the phase angle at high frequencies with rising the **H_2HEH** and **H_2MEH** concentrations indicates the growth of the adsorbed layer on the N80 steel surface.[60]

The EIS measurements of the examined components were assayed through the corresponding model shown in Fig. 5, which provided a single charge transfer reaction. The model was discovered to be in fit accordance with the obtained experimental data. The CPE was included in this model as opposed to a C_{dl} to provide a more appropriate fitting.[61] The C_{dl} that comprised a CPE exponent (Y_0 and n) were used in the formula below:[62]

$$C_{dl} = Y_0(\omega_{max})^{n-1} \quad (3)$$

where "Y_0 is the magnitude of the CPE, $\omega_{max} = 2\pi f_{max}$, f_{max} is the frequency of the imaginary element of the impedance maximum, and n is the CPE exponent defined as phase shift". The exponent n values vary between 0.611 and 0.917 ($0 < n < 1$) signifying the insufficient capacitive approach ascribed to the inhomogeneous surface as a result of the N80 surface roughness, N80 steel dissolution, the dispersion of the active sites, and the adsorption of **H_2HEH** and **H_2MEH** on the N80 steel surface.[63] From the shape of the Nyquist semicircles, it was found that the semicircles were supposed by a single capacitive semicircle. This implied that the corrosion reactions mostly followed a charge transfer mechanism.[64] The usual shape of the plots was identical for each concentration, which verified the corrosion mechanism.[65]

Table 3 provides the impedance evidence. The value of R_{ct} increased with the increase in the concentrations of **H_2HEH** and **H_2MEH**, suggesting an upturn in the inhibition efficacy (η%).

The values of C_{dl} and Y_0 diminished in the presence of the **H_2HEH** and **H_2MEH**, as can be seen from Table 3 and this reduction in the CPE/C_{dl} values was accompanied by a decrease in the local dielectric constants. The current situation is due to the exchange of water particles by **H_2HEH** or **H_2MEH** inhibitors by the adsorption process at the metal/acid interface, impeding the N80 steel corrosion.[66,67]

3.4. EFM measurements

EFM is a non-destructive method that measures the corrosion rate immediately in a short time. It can accurately provide values without having any prior knowledge of the corrosion current of the Tafel constants. Usually, the corrosion rates decided from the EFM technique are greater than the values obtained from other methods that show low corrosion rates.[68]

The intermodulation spectra acquired from EFM of the N80 steel corrosion in a 3.5% NaCl medium in the absence and presence of **H_2HEH** and **H_2MEH** are demonstrated in Fig. 6 and 7, respectively.

Table 4 summarizes the values for the corrosion kinetic variables under study at various concentrations of **H_2HEH** and **H_2MEH** in 3.5% NaCl solution at 25 ± 1 °C (i_{corr}, β_a, β_c, CF-2, CF-3, and η% calculated from eqn (1)). The corrosion current densities were reduced with the increase in the concentrations of the inhibitors. The inhibition prohibition was high at high concentrations of the **H_2HEH** and **H_2MEH**.

Table 3 Electrochemical kinetic variables attained by the EIS method for the corrosion inhibition of N80 steel in 3.5% NaCl medium before and after the addition of diverse concentrations of the synthesized hydrazides at 25 ± 1 °C

				CPE_1		CPE_2				
Comp	Conc., M	R_f, Ω cm^2	R_{ct}, Ω cm^2	Y_0, μΩ^{-1} s cm^{-2}	n	Y_0, μΩ^{-1} s cm^{-2}	n	C_{dl}, μF	θ	η%
Blank	0.00	130	565.5 ± 28.27	2.48	0.660	4.26	0.903	2.23	—	—
H_2HEH	1×10^{-6}	223	1436 ± 71.8	1.17	0.653	2.08	0.917	1.23	0.606	60.6
	5×10^{-6}	254	1785 ± 124.9	1.64	0.669	1.60	0.710	0.15	0.683	68.3
	1×10^{-5}	352	2705 ± 135.2	0.83	0.679	0.64	0.796	0.13	0.791	79.1
	5×10^{-5}	466	3238 ± 226.6	0.48	0.664	0.50	0.804	0.10	0.825	82.5
	1×10^{-4}	472	6745 ± 337.2	0.20	0.668	0.26	0.810	0.06	0.916	91.6
H_2MEH	1×10^{-6}	282	1889 ± 151.1	1.63	0.650	2.04	0.806	0.54	0.701	70.1
	5×10^{-6}	271	2012 ± 201.2	1.82	0.689	4.05	0.611	0.19	0.719	71.9
	1×10^{-5}	368	3055 ± 183.3	0.92	0.700	1.40	0.689	0.12	0.815	81.5
	5×10^{-5}	396	3875 ± 232.5	0.50	0.680	1.10	0.669	0.07	0.854	85.4
	1×10^{-4}	560	7285 ± 364.3	0.27	0.681	0.60	0.666	0.04	0.922	92.2

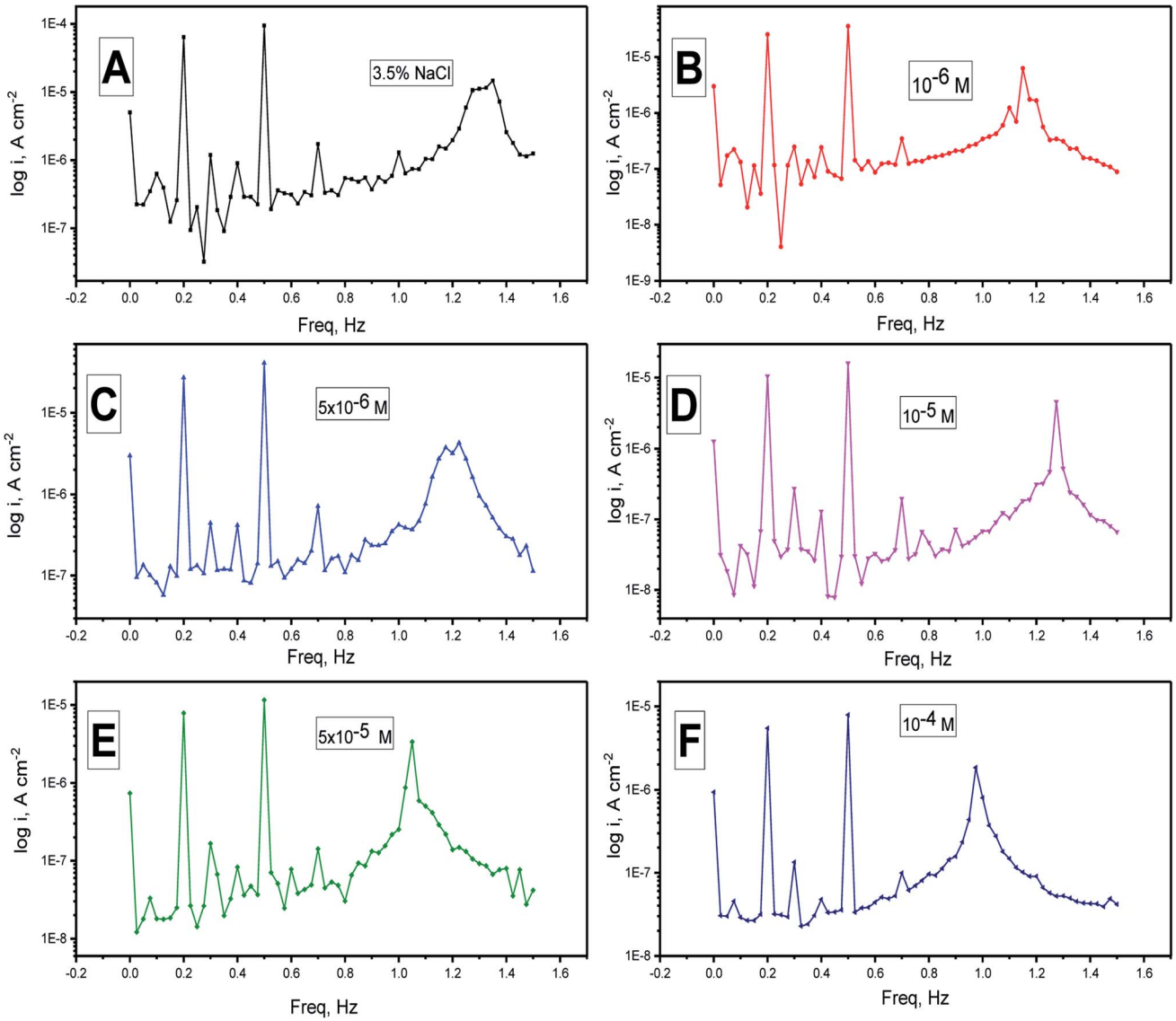

Fig. 6 (A–F) Electrochemical frequency modulation spectra for the corrosion of N80 steel in a 3.5% NaCl medium in the lack and presence of different doses of the H_2HEH at 25 °C.

The CF-2, CF-3 values are provided in Table 4. These values were not far from the expected values that were consistent with the EFM theory.[69] The values coincided with the power of the Tafel slopes and the corrosion current densities. The CF-2 and CF-3 values in Table 4 show that the evaluated values were well attributed. The regular values for CF-2 and CF-3 were 2 and 3, accordingly. The diversion of causality factors from its perfect values was most likely a result of the disturbance amplitude, which was insufficient, or the frequency spectrum resolution was low. Additionally, the inhibition was not carried out appropriately. The inhibition efficiency assessed from PP, EIS and EFM was acceptable.

3.5. Adsorption isotherm

The adsorption isotherm model was used with the assumption that the inhibition potency was mostly because of the adsorption of the inhibitor at the metal/solution interface. Adsorption isotherms for **H_2HEH** and **H_2MEH** were measured on the N80 steel surface. To achieve an isotherm model, the small surface covering values (θ) as a function of **H_2HEH** and **H_2MEH** concentration was acquired. The values of θ were obtained from PP measurements using the equation below :[70]

$$\theta = \frac{i_{corr} - i^{\circ}_{corr}}{i_{corr}} \quad (4)$$

where "i_{corr} and i°_{corr} are the corrosion current density values without and with **H_2HEH** or **H_2MEH**", respectively.

Experiments were conducted to appropriate the experimental results to different isotherms involving Freundlich (R^2 = 0.718, for **H_2HEH** and R^2 = 0.798 for **H_2MEH**), Frumkin (R^2 = 0.368, for **H_2HEH** and R^2 = 0.464 for **H2HEH**), Temkin (R^2 = 0.799, for **H_2HEH** and R^2 = 0.789 for **H2MEH**) and Flory–Huggins (R^2 = 0.842 for **H_2HEH** and R^2 = 0.889 for **H2MEH**). Most of

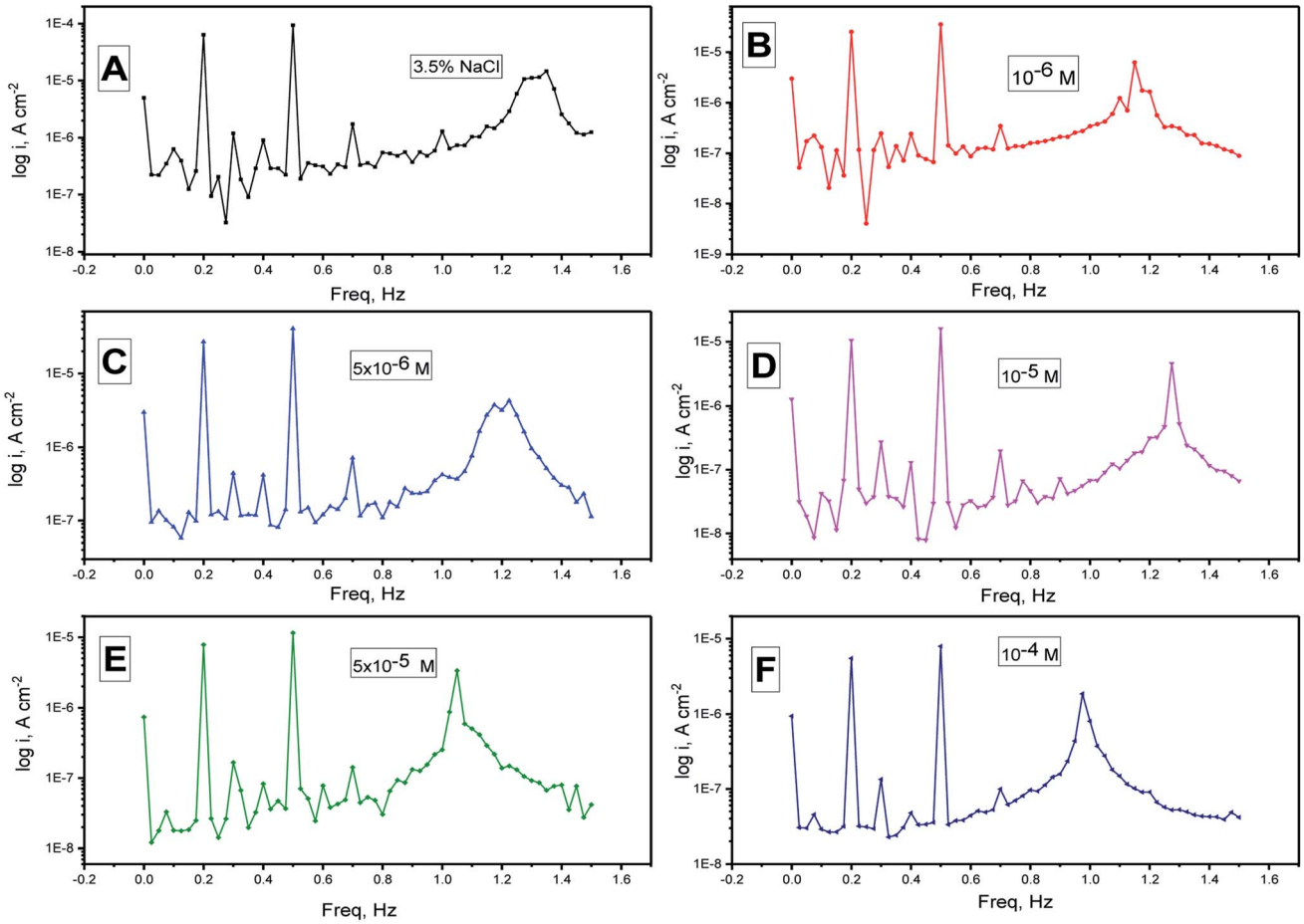

Fig. 7 (A–F) Electrochemical frequency modulation spectra for the corrosion of N80 steel in a 3.5% NaCl medium in the absence and presence of altered doses of the H_2MEH at 25 °C.

Table 4 Electrochemical kinetic variables attained by the EFM method for N80 steel in 3.5% NaCl solution holding various doses of the synthesized hydrazides at 25 °C

Comp	Conc, M	i_{corr}, μA	β_a (mV dec^{-1})	β_c (mV dec^{-1})	C.R (mpy)	CF-2	CF-3	θ	η%
Blank	0.00	132.4 ± 7.94	803	117	60.46	2.32	3.13	—	—
H_2HEH	1×10^{-6}	40.2 ± 3.87	814	109	18.34	2.01	2.13	0.696	69.6
	5×10^{-6}	36.2 ± 2.87	868	103	16.83	2.37	2.74	0.727	72.7
	1×10^{-5}	25.0 ± 2.14	815	131	11.42	2.39	3.41	0.811	81.1
	5×10^{-5}	18.9 ± 1.32	820	136	8.670	1.89	3.33	0.857	85.7
	1×10^{-4}	10.1 ± 1.01	893	103	4.596	1.70	3.18	0.924	92.4
H_2MEH	1×10^{-6}	36.7 ± 2.86	834	178	16.75	2.25	2.88	0.723	72.3
	5×10^{-6}	33.6 ± 3.36	821	132	15.32	2.26	3.19	0.746	74.6
	1×10^{-5}	23.3 ± 1.89	829	142	10.66	1.87	3.12	0.824	82.4
	5×10^{-5}	17.2 ± 1.32	816	128	7.856	2.40	2.85	0.870	87.0
	1×10^{-4}	8.4 ± 0.84	824	139	3.828	2.23	2.45	0.937	93.7

the data followed the Langmuir adsorption isotherm as evidenced in Fig. 8.[71]

$$\frac{C}{\theta} = \frac{1}{K_{ads}} + C \quad (5)$$

where "C is the concentration of **H_2HEH** and **H_2MEH**, K_{ads} is the equilibrium constant of the adsorption reaction, and θ is the surface coverage".

As shown in Fig. 8, the plot of C/θ against C showed a straight line with an adjusted coefficient of R^2, nearly equal to unity. This revealed that **H_2HEH** and **H_2MEH** followed a Langmuir isotherm and there is a small connection within the adsorbed particles. Additionally, the ΔG°_{ads}, or free energy of adsorption, were assessed using the equation below:[72]

$$\Delta G^{\circ}_{ads} = -RT \ln(55.5 K_{ads}) \quad (6)$$

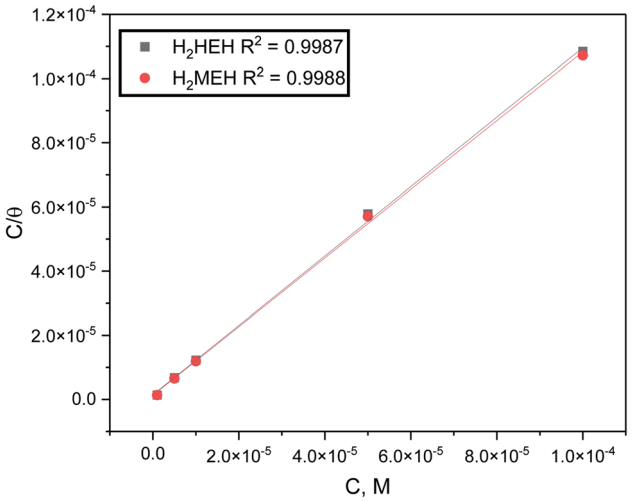

Fig. 8 Langmuir isotherm curve for N80 steel corrosion in 3.5% NaCl medium with different doses of the synthesized hydrazides at 25 °C.

Table 5 Values of K_{ads} and ΔG°_{ads} according to Langmuir isotherm

Compound	Temperature, K	$K_{ads} \times 10^4$, M^{-1}	$-\Delta G^{\circ}_{ads}$, kJmol^{-1}
H_2HEH	298	5.23	−36.87
H_2MEH	298	5.83	−37.14

where "R is the universal gas constant, T is the absolute temperature and 55. 5 is the molar concentration of water in the solution". Table 5 summarizes the values of K_{ads} and ΔG°_{ads}.

The higher values of the adsorption constant suggested strong adsorption between **H_2HEH** or **H_2MEH** and the N80 steel surface. Moreover, ΔG°_{ads} values of −36.87 and −37.14 kJ mol^{-1} demonstrated the spontaneous adsorption of the synthesized hydrazides; thus, the adsorption types on the N80 steel exterior were physisorption and chemisorption.[73]

3.6. Effect of temperature (kinetic-thermodynamic corrosion parameters)

The PP technique was used at various temperatures from 25 °C to 50 °C with 1 × 10^{-4} M of **H_2HEH** or **H_2MEH** (Fig. 9). The corrosion rates increased with the upsurge in temperature (Table 6). The corrosion rate of N80 steel without the compounds under study increased sharply from 25 °C to 50 °C. In the occurrence of the inhibitors, the corrosion rates reduced gradually. The prohibition potency was reduced by the increase in temperature indicating the physisorption of the additives on the N80 steel surface. Table 6 summarizes the corrosion parameters with and without the inhibitors in the temperature region of 25–50 °C. The inhibition prohibition was reduced with the increment in the temperature. The activation energy (E^{*}_{a}) for the dissolution of the N80 steel in a 3.5% NaCl corrosive

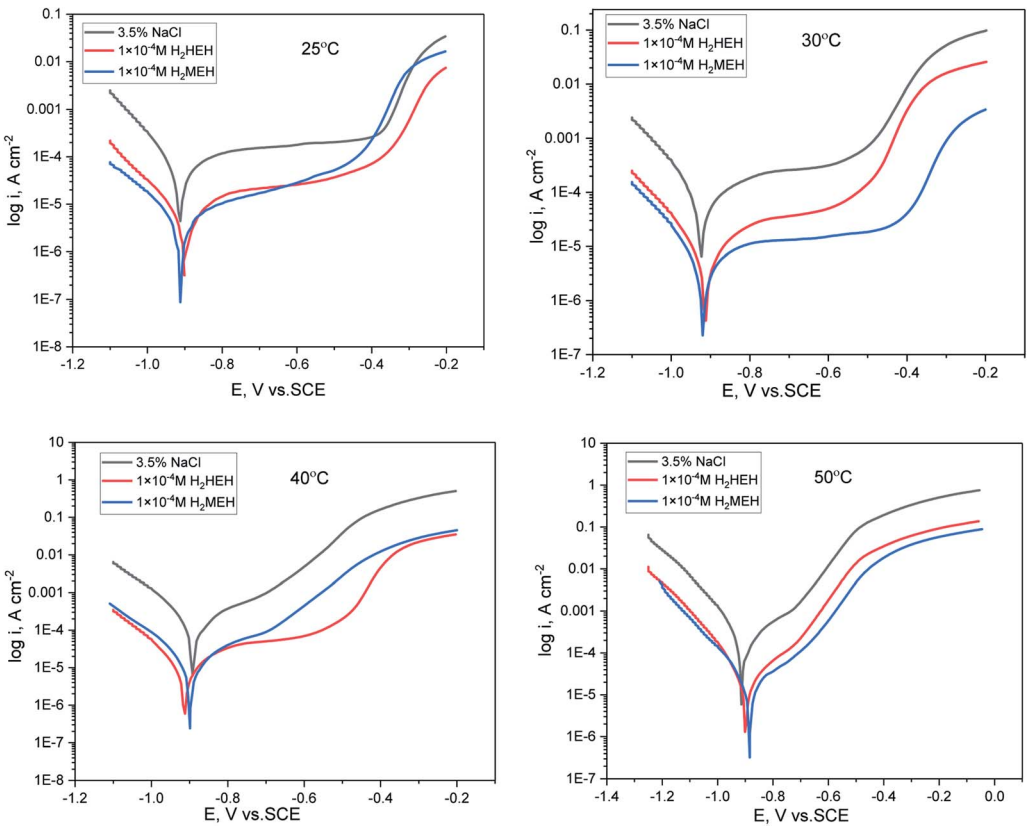

Fig. 9 Anodic and cathodic polarization plots for the corrosion of N80 steel in 3.5% NaCl solution in the lack and existence of 1 × 10^{-4} M concentration of the synthesized hydrazides.

Table 6 The electrochemical variables designed *via* the potentiodynamic polarization method for the corrosion inhibition of N80 steel in 3.5% NaCl solution and including 1×10^{-4} M concentration of the synthesized hydrazides in the range 25–50 °C

Temp, C°	Compound	$-E_{corr}$, mV	i_{corr}, μAcm^{-2}	β_a, mV dec^{-1}	β_c, V dec^{-1}	C.R. mmy^{-1}	θ	η%
25	Blank	915	113.0	1512	152	51.46	—	—
	H_2HEH	902.0	8.8	613	150	4.02	0.877	87.7
	H_2MEH	911.0	7.6	524	182	3.45	0.922	92.2
30	Blank	925.0	126.0	700	134	57.33	—	—
	H_2HEH	914.0	14.1	536	154	6.44	0.788	78.8
	H_2MEH	919.0	10.6	1858	158	4.86	0.841	84.1
40	Blank	893.0	161.0	233	123	73.42	—	—
	H_2HEH	914.0	18.6	511	149	8.49	0.729	72.9
	H_2MEH	900.0	13.6	210	130	6.19	0.790	79.0
50	Blank	915.0	189.0	244	115	86.33	—	—
	H_2HEH	899.0	20.4	177	117	9.32	0.729	72.9
	H_2MEH	885.0	15.8	196	129	7.23	0.790	79.0

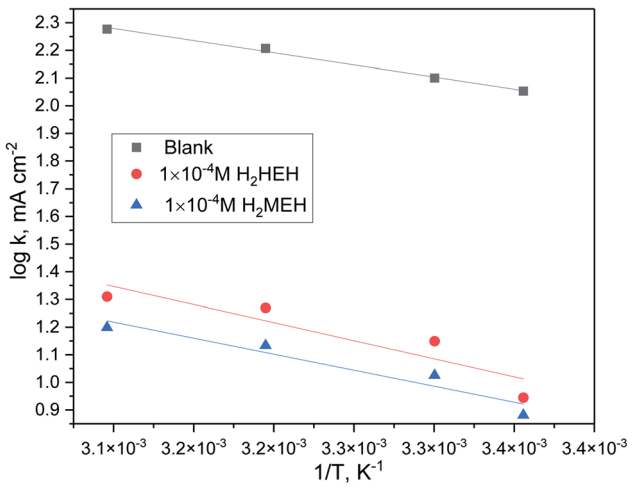

Fig. 10 log *k* (corrosion rate) *vs.* 1/*T* plot for N80 steel in 3.5% NaCl medium in the lack and existence of 1×10^{-4} M concentration of the investigated hydrazides.

Table 7 Activation variables for the dissolution of N80 steel without and with 1×10^{-4} M concentration of the synthesized hydrazides in 3.5% NaCl medium in the temperature range of 25–50 °C

Compound	E_a^*, kJmol^{-1}	ΔH^*, J mol^{-1}	$-\Delta S^*$, J mol^{-1}
Blank	16.79	6.17	157.92
H_2HEH	25.03	9.75	150.24
H_2MEH	22.21	8.52	161.43

medium was studied using the slope of the diagrams by the Arrhenius equation below.

$$\log k = \frac{-E_a^*}{2.303RT} + \log A \quad (7)$$

where "*k* is the corrosion rate, E_a^* is the activation energy, *R* is the universal gas constant, *T* is the absolute temperature and *A* is the Arrhenius pre-exponential element".

By designing (log *k*) *versus* (1/*T*), the values of E_a^* were acquired from the previous equation: $(E_a^* = (\text{slope})2.303 \times R)$ (Fig. 10). The activation energy for the corrosion of N80 C-steel in 3.5% NaCl corrosive solution increased in the attendance of **H_2HEH** and **H_2MEH** (Table 7). The increase in E_a^* suggested a structure of energy obstruction. The rate augments in the

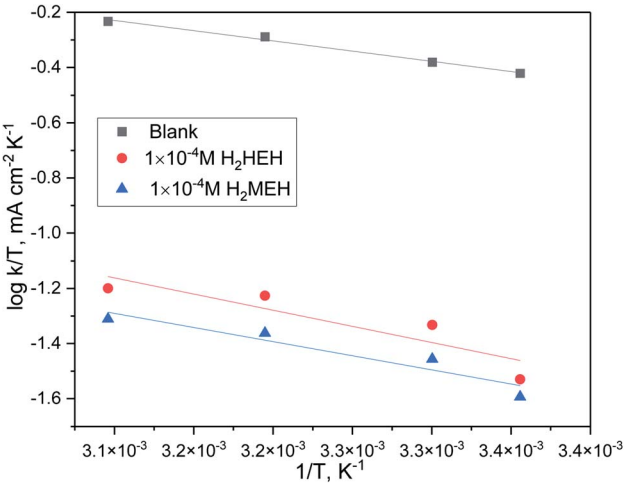

Fig. 11 log *k* (corrosion rate)/*T* *vs.* 1/*T* plot for N80 steel in 3.5% NaCl medium and including 1×10^{-4} M concentration of the investigated hydrazides.

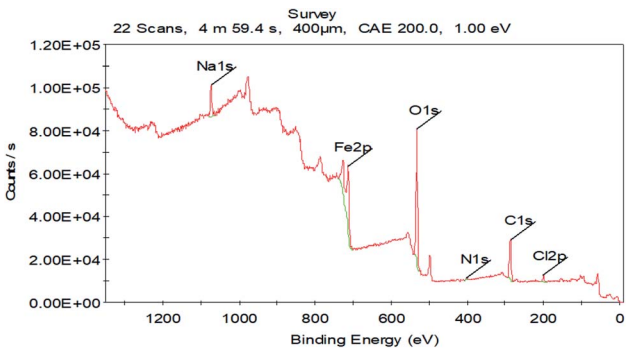

Fig. 12 XPS survey obtained for N80 steel in 3.5% NaCl treated with 1×10^{-4} M of **H_2MEH**.

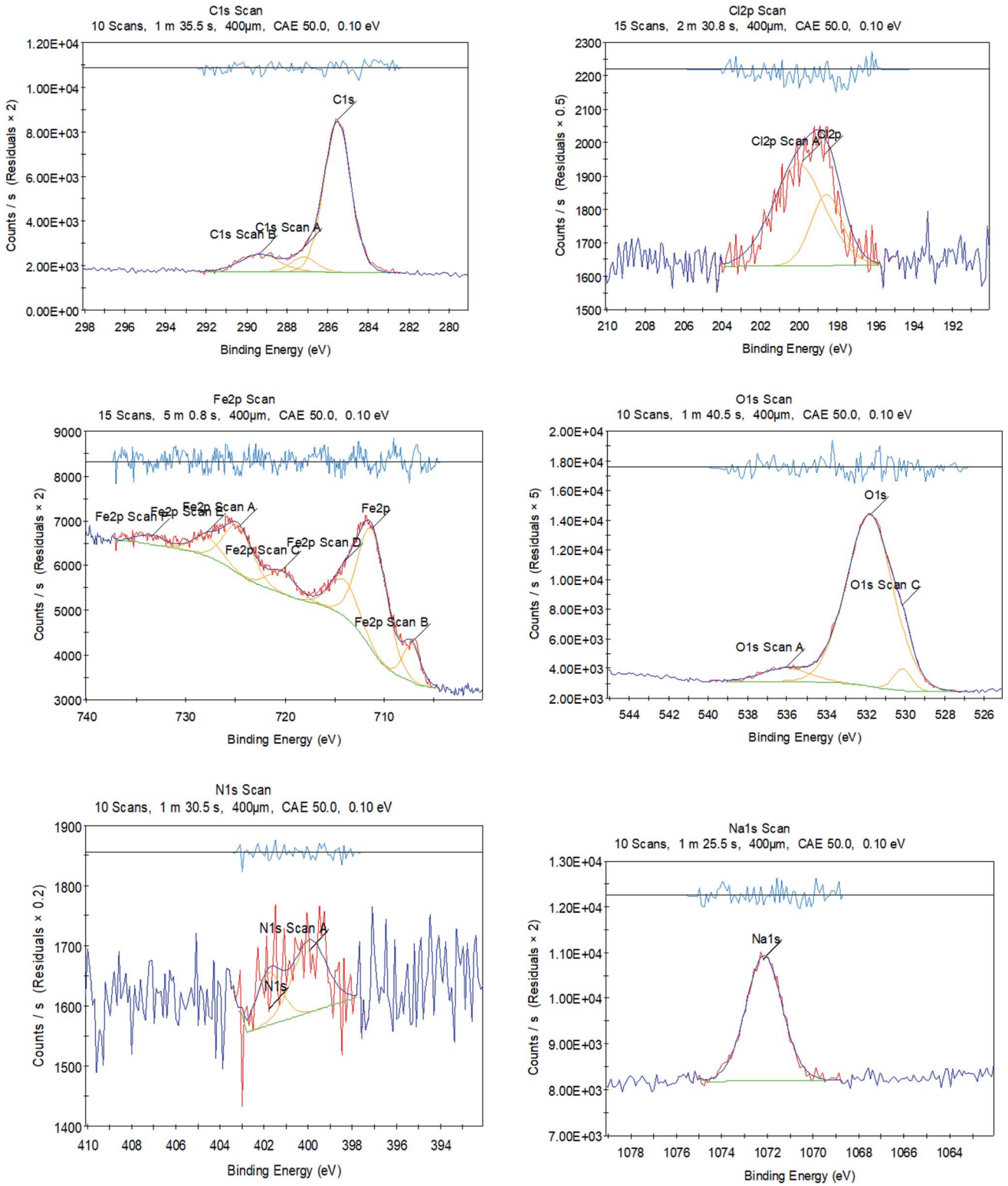

Fig. 13 XPS outlines of C 1s, Cl 2p, Fe 2p, O 1s, N 1s, and Na 1s for N80 steel in 3.5% NaCl treated with 1×10^{-4} M of H_2MEH.

existence of the inhibitors were higher than those in the absence of corrosive media. Thus, the prohibition tendency of **H_2HEH** and **H_2MEH** lessened with a rise in the temperature.

The above outcomes supported the physical nature of the adsorption of **H_2HEH** and **H_2MEH** on an N80 steel surface. The rise in the temperature decreased the number of adsorbed particles, thus, decreasing the inhibition efficiency. The inhibitors prevent the corrosion process by increasing the activation energy. The adsorption process on the N80 steel exterior was by a charge transfer mechanism. These inhibitors also serve as

Table 8 Binding energies (eV) and their assignments for the principal core lines discovered in 3.5% NaCl treated with 1×10^{-4} M H_2MEH for the N80 steel surface

N80 steel in 3.5% NaCl treated with 1×10^{-4} M **H_2MEH**		
Core element	BE, eV	Assignments
C 1s	285.51	–C–H, –C–C–, –C=C–
	287.55	–C–O
	289.36	–C=N^+
Cl 2p	198.66	Cl $2p_{3/2}$
	199.78	Cl $2p_{1/2}$
Fe 2p	707.23	Fe $2p_{3/2}$ of Fe^0
	711.20	Fe $2p_{3/2}$ of Fe^{2+} in FeO, $FeCl_2$
	714.06	Fe $2p_{3/2}$ of Fe^{3+} in Fe_2O_3, Fe_3O_4, FeOOH
	720.26	Satellite Fe $2p_{3/2}$ of Fe^{2+} in FeO
	724.71	Fe $2p_{1/2}$ of Fe^{2+} in FeO
	727.91	Fe $2p_{1/2}$ of Fe^{3+} in Fe_2O_3
	733.48	Satellite Fe $2p_{1/2}$ of Fe^{2+} in Fe_2O_3, Fe_3O_4
O 1s	530.14	FeO, Fe_2O_3
	531.80	FeOOH
	536.03	Adsorbed water molecules
N 1s	399.94	–C=N
	401.07	–C=N^+
Na 1s	1072.15	Na in NaCl

building blocks for mass. Furthermore, the rather small activation energy values for **H_2HEH** and **H_2MEH** implied a physical adsorption mechanism.

The change of entropy (ΔS^*) and change of enthalpy (ΔH^*) were calculated utilizing the equation below:

$$k = \left(\frac{RT}{N_a h}\right)\exp\left(\frac{\Delta S^*}{R}\right)\exp\left(\frac{\Delta H^*}{RT}\right) \quad (8)$$

whereas "k is the value for the corrosion rate, h is Planck's constant and N_a is Avogadro number". The relationship of $\log(k/T)$ to $1/T$ (Fig. 11) was considered a straight line, with a slope and intercept of $(\Delta H^*/2.303R)$ and $[\log(R/N_a h) + \Delta S^*/2.303R]$, respectively. Table 7 summarizes the calculated values of ΔS^* and ΔH^*. The negative value of ΔS^* showed an activated complex as the rate-determining step. A reduction in the disorder occurred, which was within the path of the transition from reactants to products.[74] The exothermic process indicated whether physisorption, chemisorption, or a combination of both.

3.7. XPS studies

The XPS investigation was used to distinguish the chemical composition and bonding in an **H_2MEH** molecule. It was used to ascertain the adsorption of the **H_2MEH** compound on an N80 steel surface and clarify the corrosion inhibition mechanism. The XPS results obtained for treating the N80 steel surface with 1×10^{-4} M **H_2MEH** and corroded in 3.5% NaCl are shown in Fig. 12. Meanwhile, Fig. 13 shows the XPS of C 1s, Fe 2p, O 1s, N 1s, and Na 1s for the treated N80 steel sample. Table 8 shows the binding energies (BE) (eV) and the equivalent designation for any peak component.

The involved spectra of C 1s displayed three peaks (Fig. 13), including that for the inhibited N80 steel at 285.51, which was assigned to –C–C–, –C=C–, and C–H bonds. The 287.19 eV and 289.36 eV peaks are ascribed to –C–O, and –C=N^+ bonds, respectively.[75,76] The deconvolution of the Cl 2p spectra divulged into two peaks (Fig. 13) at 198.6 and 199.78 eV, which were assigned to Cl $2p_{3/2}$ and Cl $2p_{1/2}$, respectively.[77] The XPS spectra of Fe 2p showed seven peaks (Fig. 13) at 707.23 eV for Fe $2p_{3/2}$ of Fe^0, 711.20 eV for Fe $2p_{3/2}$ of Fe^{2+}, 714.06 eV for Fe $2p_{3/2}$ of Fe^{3+},[77] 720.01 eV for Fe $2p_{3/2}$ satellites of Fe^{2+},[78] 724.36 eV for Fe $2p_{1/2}$ of Fe^{2+}, 727.91 eV for Fe $2p_{1/2}$ of Fe^{2+}, and 733.48 eV for Fe $2p_{1/2}$ satellites of Fe^{2+}.[79,80] Furthermore, the high-resolution O 1s spectrum showed three peaks (Fig. 13), including 530.14 eV for O^{2-} that interacted with $Fe^{2+}$and Fe^{3+} to form FeO and Fe_2O_3 oxides.[81,82] The 531.80 and 536.03 eV were for the OH^- that interacted with Fe^{3+} to form FeOOH and adsorbed water molecules, respectively.[83,84]

The N80 steel treated with **H_2MEH** in 3.5% NaCl exhibited two N 1s peaks (Fig. 13) at 399.94 and 401.75 eV, which were ascribed to –C=N and –C=N^+ bonds, respectively. These were due to the **H_2MEH** molecules.[85,86] Finally, a distinctive Na 1s peak (Fig. 13) observed at 1072.15 eV was assigned to Na in the NaCl solution.[87] These results verified the adsorption of **H_2MEH** on the N80 steel exterior. These compound created a durable shielding layer.

3.8. DFT studies

Fig. 14 shows the optimized structures, including the HOMO and LUMO distributions for the hydrazide derivatives. Table 9 presents the corresponding quantum chemical descriptors. As suggested by the frontier orbital theory, the donor or acceptor interactions at the interface between the inhibitor compound and metal exterior are described by the HOMO and LUMO energies.[88] Thus, high and low values for E_{HOMO} and E_{LUMO}, respectively, suggest a corrosion prohibition, which is enhanced by the presence of the compounds under study. In Table 9, **H_2MEH** has a higher HOMO value of −4.86 eV when compared with **H_2HEH** (−5.26 eV). As shown in Fig. 14, the HOMO levels for hydrazide were located at the methoxy, hydroxy, carbonyl and phenyl rings, suggesting that the nitrogen and oxygen atoms were the favored positions for electrophilic attacks on the metal exterior. This could enhance the prohibition caused by the hydrazide derivatives by the adsorption on the N80 exterior, thus, enhancing the prohibition potency. This concurred with the data observed. In contrast, the E_{LUMO} value was −2.95 eV for **H_2MEH** (Table 9), which was less than −0.68 eV for **H_2HEH**. This also agreed with the experimental results, where better protection power was observed for **H_2MEH**.

The energy gap (ΔE) is an essential element to assist the inhibition potency of the hydrazides for corrosion. Lower ΔE values suggested better inhibition potencies.[89] As evidenced in Table 9, **H_2MEH** has a lower ΔE value (1.91 eV) than **H_2HEH** (2.58 eV). This implied a higher tendency for **H_2MEH** adsorption on a C-steel exterior. The smaller values of electronegativity (χ) for **H_2MEH** suggested the stronger ability of **H_2MEH** than **H_2HEH** to provide electrons to the metal.[90] The stability and reactivity of a compound could also be used to evaluate its hardness (η) and softness (σ). Soft compounds are highly

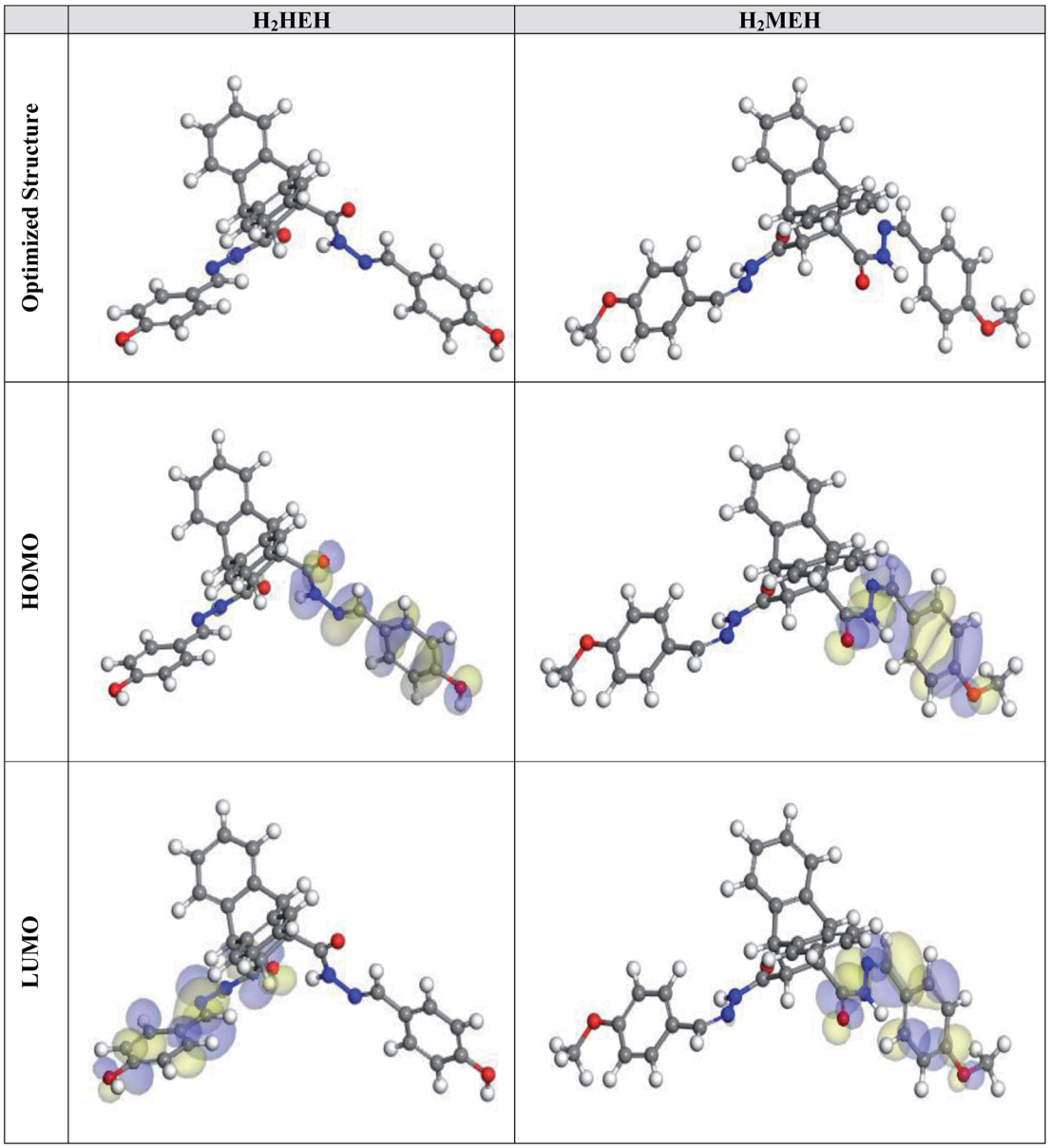

Fig. 14 The optimized molecular constructions, HOMO and LUMO for the synthesized hydrazides *via* the DMol^3 module.

Table 9 Quantum chemical parameters calculated for synthesized hydrazide molecules

Compound	H_2HEH	H_2MEH
E_{HOMO}, eV	−5.26	−4.86
E_{LUMO}, eV	−2.68	−2.95
ΔE, eV	2.58	1.91
I	5.26	4.86
A	2.68	2.95
χ	3.97	3.91
η	1.29	0.96
σ	0.78	1.05
ΔN	1.18	1.21
Dipole moment, debye	7.04	7.20
Molecular surface area, Å^2	498.89	553.87

reactive than hard compounds and they effortlessly provide electrons to an N80 sample during the adsorption. Thus, they work as effective corrosion inhibitors.[91] As shown in Table 9, the **H_2MEH** has a higher σ value (1.05) and **H_2HEH** has a lower η value (0.96). This indicated the ability of **H_2MEH** to easily provide electrons to the examined sample. This produced a high prohibition potency.

The ΔN values showed the tendency of a particle to donate electrons to the surface. A high ΔN value, suggests a larger electron-donating ability of an inhibitor. It has been found that when $\Delta N < 3.6$, the prohibition performance was enhanced because of the high electron-contributing ability.[92] Table 9 lists the calculated values of ΔN. The higher ΔN values for **H_2MEH** (1.21) than for **H_2HEH** (1.18) suggested that **H_2MEH** had a higher tendency to donate electrons to the examined sample.

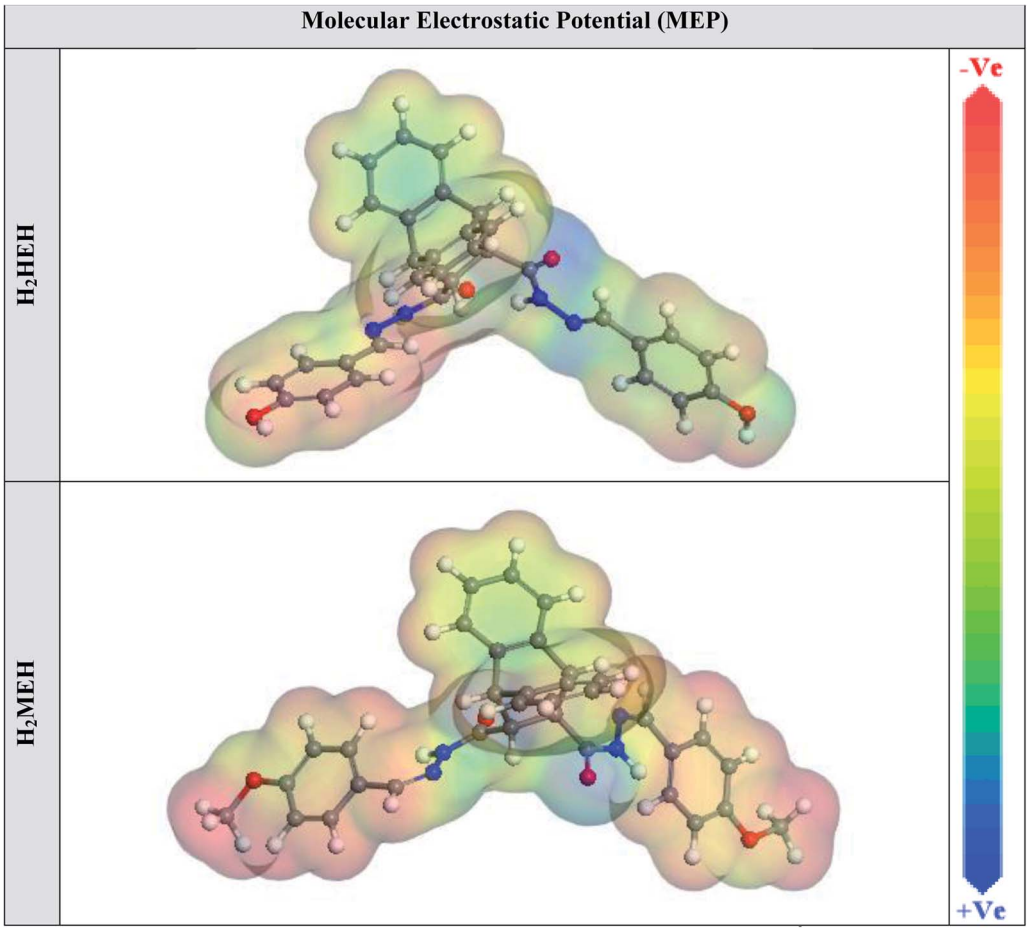

Fig. 15 MEP graph of the synthesized hydrazides by the DMol^3 module.

The dipole moment is a vigorous element that confirms a corrosion prohibition.[93] A rise in a dipole moment suggests an improvement in the deformation energy and enhancement in the adsorption of an inhibitor on the steel surface. Thus, a rise in the dipole moment will increase the prohibition efficacy.[94] As shown in Table 9, the dipole moment of **H_2MEH** (7.20 debye) is higher than **H_2HEH** (7.04 debye). This verified the higher tendency for **H_2MEH** adsorption on the N80 surface, causing an improved prohibition potency.

Additionally, a visible correlation was found between the molecular surface area of the hydrazides and their tendency to protect the N80 surface in a 3.5% NaCl medium. A larger surface area improves the prohibition potency since the contact area on the N80 surface becomes larger for the hydrazides.[95] As shown in Table 9, **H_2MEH** showed a larger molecular surface area (553.87 Å^2), thus, it provided a better prohibition potency than **H_2HEH**.

The MEP mapping in a 3D visual device is designed to recognize the optimum electrostatic result, which is calculated over a particle from the total charge dispersion.[96] In the MEP maps shown in Fig. 15, the red regions delineated the greatest electron density, where MEP is the most negative (nucleophilic reaction). Meanwhile, the blue regions delineate from the highest positive area (electrophilic reaction).[97] The photograph in Fig. 15 shows the most negative areas were from hydrazide at the methoxy, hydroxy and carbonyl rings. Nevertheless, a lower density at the phenyl rings was observed. The red spots with high electron density in the hydrazides were the suitable connections on the N80 surface for building an adsorbed protective film.

3.9. MC simulations

MC simulations were used to perceive the interactions between the hydrazides and the C-steel surface and the mechanism of adsorption. Fig. 16 shows the most likely adsorption configurations for the hydrazides on the N80 sample. This was achieved by the adsorption locator module that presents the smooth disposition, and suggests an improvement in the adsorption with the highest surface coverage.[98] Moreover, Table 10 summarizes the calculations from the Monte Carlo simulations. The table lists the adsorption energies for relaxed adsorbate compounds, rigid adsorption energies for unrelaxed adsorbate compounds, and deformation energies for relaxed adsorbate compounds.[99] The **H_2MEH** showed a more negative value for adsorption energy (−2649.11 kcal mol^{-1}) compared with **H_2HEH** (−2636.23 kcal mol^{-1}). This proved the stronger adsorption of **H_2MEH** on the C-steel surface, making a steady

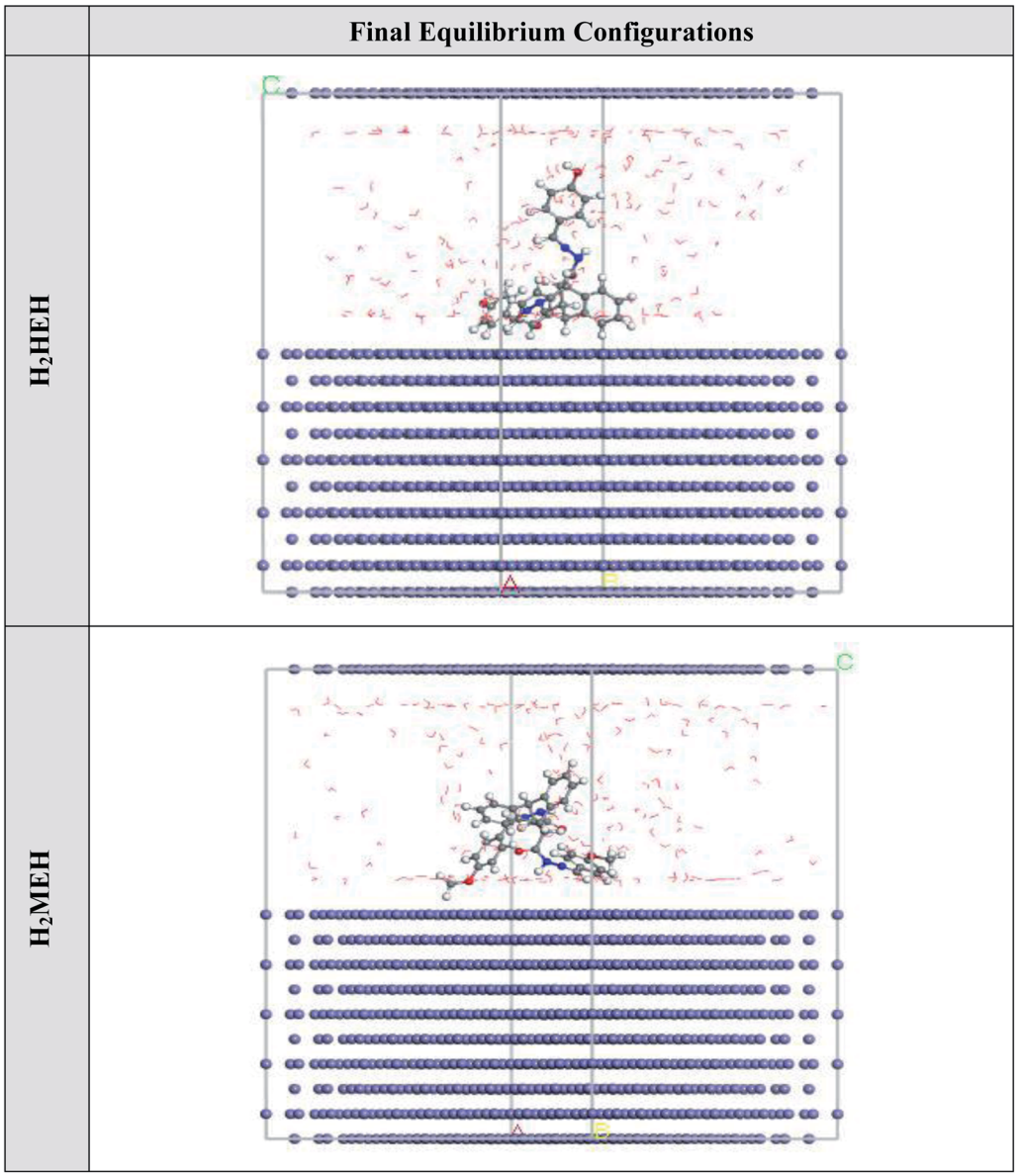

Fig. 16 The adsorption locator module achieved the maximal suitable conformation for the adsorption of the synthesized hydrazides on Fe (1 1 0) substrate.

Table 10 Data and descriptors obtained using the Monte Carlo simulation for the adsorption of H_2MEH and H_2HEH compounds on Fe (1 1 0)[a]

Structures	Adsorption energy/ kcal mol^{-1}	Rigid adsorption energy/kcal mol^{-1}	Deformation energy/ kcal mol^{-1}	dE_{ads}/dN_i:inhibitor/ kcal mol^{-1}	dE_{ads}/dN_i:water/ kcal mol^{-1}
Fe (1 1 0) **H_2HEH** Water	−2636.23	−2756.00	119.77	−178.65	−13.73
Fe (1 1 0) **H_2MEH** Water	−2649.11	−2771.19	122.08	−194.77	−13.88

[a] The energy of the metal adsorbate arrangement, where the energy of the adsorbates was neglected is elucidated by dE_{ads}/dN_i values.[100] The dE_{ads}/dN_i values for **H_2MEH** was −194.77 kcal mol^{-1}, which was higher than the value for **H_2HEH** molecules of −178.65 kcal mol^{-1}, which affirmed stronger adsorption of **H_2MEH** than **H_2HEH**. Besides, the dE_{ads}/dN_i value for water molecules is 13.81 kcal mol^{-1}, suggesting the stronger adsorption of hydrazides than water. Hence, the hydrazides were conclusively adsorbed on the N80 surface and formed an effective protective barrier.

Table 11 Comparison between our results and formerly published studies on using hydrazide derivatives as corrosion inhibitors

Inhibitor used	Examined metal	Corrosive media	Inhibition efficiency	Reference
Ferrocene Schiff bases derived from hydrazides	Mild steel	In 0.5 M, H_2SO_4	91.1% EIS	102
Sulfonohydrazide derivatives	XC38 carbon steel	1 M HCl	91.9% polarization, 93.1% EIS	34
Hydroxy phenyl hydrazides	Mild steel	1 M HCl solution	92.41% EIS, 92.4% weight loss	35
Cationic Gemini surfactant	X-65 steel	1.0 M HCl	91.44% EIS, 94.73% EIS	103
Organic acid hydrazides	Mild steel	1.0 M HCl	93.8% weight loss, 81.3% polarization	32
2-(2-Hydrazinyl-1,6-dihydro-6-oxopyrimidin-4-yl) acetohydrazide	Mild steel	M HCl and 0.5 M H_2SO_4	89.8% polarization in HCl, 88.5% polarization in H_2SO_4	37
Polymeric hydrazide derivatives	Mild steel	1 M HCl	93.97% polarization	104
Novel dicarbohydrazide derivatives	N80 steel	3.5% NaCl solution	93.3% polarization, 92.2% EIS	Our current study

adsorbed barrier that prevents the C-steel corrosion. These results agree with the practical data. The values for adsorption energy for **H_2MEH** at pre-and post-geometry optimization stages *i.e.*, unrelaxed and relaxed were −2771.19 and 122.08 kcal mol^{-1}, respectively. These values were more negative than **H_2HEH**, suggesting a greater prohibition tendency for **H_2MEH** than for **H_2HEH**.

3.10. Mechanism of inhibition of hydrazide derivatives and comparison of the inhibition efficiencies of our study derivatives with those of previous studies

The mechanism of corrosion inhibition has several parts mechanism and is linked to the construction of a preventive/adsorbed layer on the examined metal. The procedure of adsorption was monitored by various variables, which are stated below:[101]

(a) There were interactions between **H_2HEH** or **H_2MEH** and the substrate.

(b) The investigated molecules combined on the metal layer.

(c) There were chemical processes involved.

(d) The electrode potentials were relevant.

(e) The doses of the examined inhibitors were relevant.

(f) The temperature of the system was important.

(g) The characteristics of the metal exterior were important.

The adsorption of the synthesized **H_2HEH** and **H_2MEH** on the N80 steel metal can occur instantly by virtue of donor–acceptor correlations with N or O atoms of the compounds and the presence of free d- orbitals in N80 steel particles.

The **H_2HEH** and **H_2MEH**, including their electronegative atoms, were frequently reported to have a large ability to contribute electrons to an N80 steel surface.[49] Thus, the interaction between **H_2HEH** and **H_2MEH** and the exterior of the N80 steel involved the electronegative atoms of the inhibitors. The localities of higher electron density are common spots for electrophiles attack. Therefore, N and O atoms with energetic sites, have the greatest capability to bond with the N80 steel exterior.

The prohibition tendency of **H_2MEH** was better than that of **H_2HEH**.

H_2MEH provided a higher inhibition efficiency percentage, which was a result of the existence of *p*-OCH_3, which is an electron-contributing group in its structure. This group increased the electron charge density on the inhibitor. The lower efficiency in **H_2HEH** was due to the H-atom in the *p*-position, which has no purpose in the charge density of the compound.

In conclusion, the sites with electron-donating groups (–N and –O atoms) were the most likely spots for bonding of **H_2HEH** and **H_2MEH** on the metal surface. Additionally, the findings from quantum chemical calculations provided excellent matching with the collected data from the electrochemical techniques and adsorption of the synthesized compounds. These findings were mostly focused on the relevance of nitrogen and oxygen atoms.

Finally, Table 11 demonstrates a comparison between our results and previously the published studies on corrosion inhibition utilizing hydrazide derivatives in different corrosive mediums.

4. Conclusions

In this work, we synthesized and characterized novel **H_2HEH** and **H_2MEH** hydrazide derivatives. The molecular composition of the compounds was determined using FT-IR, NMR spectroscopy, and electronic spectra. The corrosion prohibition on N80 steel using the hydrazides was studied by electrochemical techniques of PP, EIS and EFM and theoretical calculations. The following are the highlights of the study.

(1) Data collected from the electrochemical methods and theoretical calculations indicated that the synthesized hydrazides served as powerful compounds for N80 carbon steel corrosion in a 3.5% NaCl solution.

(2) Prohibition tendency enhanced with the rise in the concentration of the examined hydrazides. It decreased with an increase in the temperature.

(3) The prohibition efficiency, which was measured using PP, EIS and EFM was in a respectable arrangement.

(4) PP measurements showed that the synthesized hydrazides behaved as a mixed-type inhibitor.

(5) XPS studies affirmed the formation and creation of a durable shielding layer, which protected the exterior of the N80 carbon steel from corrosion.

(6) The synthesized hydrazides were adsorbed on the N80 carbon steel surface in a 3.5% NaCl corrosive medium. The adsorption was an exothermic process, which indicated both physisorption and chemisorption, and followed the Langmuir adsorption isotherm.

(7) These findings demonstrate the superior performance of the prepared **H_2HEH** and **H_2MEH** hydrazide derivatives as inhibitors for N80 carbon steel corrosion and accordingly prove their favorability for the protection of steel in aggressive chloride solutions. Due to the unique structure of these compounds, they can be applied as effective inhibitors during the acid pickling process.

Conflicts of interest

The authors declare that they have no known competing financial interests or personal relationships that could have appeared to influence the work reported in this paper.

Acknowledgements

This work was supported through the Annual Funding track by the Deanship of Scientific Research, Vice Presidency for Graduate Studies and Scientific Research, King Faisal University, Saudi Arabia [GRANT-609].

References

1 X. Li, S. Deng and H. Fu, *Corros. Sci.*, 2011, **53**, 302–309.
2 B. Labriti, N. Dkhireche, R. Touir, M. Ebn Touhami, M. Sfaira, A. El Hallaoui, B. Hammouti and A. Alami, *Arab. J. Sci. Eng.*, 2012, **37**, 1293–1303.
3 S. Javadian, A. Yousefi and J. Neshati, *Appl. Surf. Sci.*, 2013, **285**, 674–681.
4 A. A. Gurten, E. Bayol, K. Kayakirilmaz and M. Erbil, *Steel Compos. Struct.*, 2009, **9**, 77–87.
5 M. Raupach, B. Elsener, R. Polder and J. Mietz, *Corrosion of Reinforcement in Concrete: Monitoring, Prevention and Rehabilitation Techniques, A volume in European Federation of Corrosion (EFC) Series*, 2007.
6 T. A. Söylev and M. G. Richardson, *Construct. Build. Mater.*, 2008, **22**, 609–622.
7 H. E. Jamil, M. F. Montemor, R. Boulif, A. Shriri and M. G. S. Ferreira, *Electrochim. Acta*, 2003, **48**, 3509–3518.
8 A. H. Tantawy, K. A. Soliman and H. M. Abd El-Lateef, *J. Clean. Prod.*, 2020, **250**, 119510.
9 M. Behpour, S. M. Ghoreishi, N. Soltani and M. Salavati-Niasari, *Corros. Sci.*, 2009, **51**, 1073–1082.
10 A. Y. Yassin, A. M. Abdelghany, M. M. Shaban and Y. M. Abdallah, *Colloids Surf. A Physicochem. Eng. Asp.*, 2022, **635**, 128115.
11 M. Behpour, S. M. Ghoreishi, N. Soltani, M. Salavati-Niasari, M. Hamadanian and A. Gandomi, *Corros. Sci.*, 2008, **50**, 2172–2181.
12 A. K. Singh, B. Chugh, S. Thakur, B. Pani, H. Lgaz, I.-M. Chung, S. Pal and R. Prakash, *Colloids Surf. A Physicochem. Eng. Asp.*, 2020, **599**, 124824.
13 B. Chugh, A. K. Singh, S. Thakur, B. Pani, A. K. Pandey, H. Lgaz, I.-M. Chung and E. E. Ebenso, *J. Phys. Chem. C*, 2019, **123**, 22897–22917.
14 B. Chugh, A. K. Singh, D. Poddar, S. Thakur, B. Pani and P. Jain, *Carbohydr. Polym.*, 2020, **234**, 115945.
15 R. Wang, G. Qin and E. Zhang, *J. Mater. Sci. Technol.*, 2020, **52**, 127–135.
16 S. Wan, X.-Z. Ma, C.-H. Miao, X.-X. Zhang and Z.-H. Dong, *Corros. Sci.*, 2020, **170**, 108692.
17 H. Huang and X. Guo, *Colloids Surf. A Physicochem. Eng. Asp.*, 2020, **598**, 124809.
18 S. Rangelov and V. Mircheva, *Corros. Sci.*, 1996, **38**, 301–306.
19 K. F. Khaled, *Appl. Surf. Sci.*, 2006, **252**, 4120–4128.
20 M. Nasr-Esfahani, M. Zendehdel and B. Jafari, *Prot. Met. Phys. Chem. Surf.*, 2015, **51**, 285–294.
21 A. Singh, K. R. Ansari, D. S. Chauhan, M. A. Quraishi, H. Lgaz and I.-M. Chung, *J. Colloid Interface Sci.*, 2020, **560**, 225–236.
22 A. K. Singh, A. K. Pandey, P. Banerjee, S. K. Saha, B. Chugh, S. Thakur, B. Pani, P. Chaubey and G. Singh, *J. Environ. Chem. Eng.*, 2019, **7**, 102971.
23 P. Molaeipour, M. Ramezanzadeh and B. Ramezanzadeh, *Bioelectrochemistry*, 2022, **143**, 107970.
24 L. Cheng, C. Liu, H. Wu, H. Zhao and L. Wang, *J. Colloid Interface Sci.*, 2022, **606**, 1572–1585.
25 A. H. J. Mofidabadi, A. Dehghani and B. Ramezanzadeh, *Colloids Surf. A Physicochem. Eng. Asp.*, 2021, **630**, 127561.
26 T. Attar, F. Nouali, Z. Kibou, A. Benchadli, B. Messaoudi, E. Choukchou-Braham and N. Choukchou-Braham, *J. Chem. Sci.*, 2021, **133**, 109.
27 T. Laabaissi, M. Rbaa, F. Benhiba, Z. Rouifi, U. P. Kumar, F. Bentiss, H. Oudda, B. Lakhrissi, I. Warad and A. Zarrouk, *Colloids Surf. A Physicochem. Eng. Asp.*, 2021, **629**, 127428.
28 K. O. Sulaiman and A. T. Onawole, *Comput. Theor. Chem.*, 2016, **1093**, 73–80.
29 R. Schliebs, *Angew. Chem., Int. Ed.*, 1985, **24**, 1006–1007.
30 M. Nassiri Koopaei, M. J. Assarzadeh, A. L. I. Almasirad, S. F. Ghasemi Niri, M. Amini, A. Kebriaeezadeh, N. Nassiri Koopaei, M. Ghadimi and A. Tabei, *Iran. J. Pharm. Res.*, 2013, **12**, 721–727.
31 E. F. Rothgery, Hydrazine and Its Derivatives., *Kirk-Othmer Encycl. Chem. Technol.*, 2004, DOI: **10.1002/0471238961.0825041819030809.a01.pub2**.
32 M. A. Quraishi, R. Sardar and D. Jamal, *Mater. Chem. Phys.*, 2001, **71**, 309–313.
33 P. Preethi Kumari, P. Shetty and S. A. Rao, *Arab. J. Chem.*, 2017, **10**, 653–663.

34 I. Ichchou, L. Larabi, H. Rouabhi, Y. Harek and A. Fellah, *J. Mol. Struct.*, 2019, **1198**, 126898.
35 A. K. Singh, B. Chugh, M. Singh, S. Thakur, B. Pani, L. Guo, S. Kaya and G. Serdaroglu, *J. Mol. Liq.*, 2021, **330**, 115605.
36 S. V Ramesh and A. V. Adhikari, *Mater. Chem. Phys.*, 2009, **115**, 618–627.
37 Z. A. Abdallah, M. S. Mohamed Ahmed and M. M. Saleh, *Mater. Chem. Phys.*, 2016, **174**, 91–99.
38 K. I. Aly, A.-E.-W. A. Sarhan and T. I. El-Emary, *Arab. J. Chem.*, 2010, **3**, 61–68.
39 S. S. Abdel-Rehim, K. F. Khaled and N. S. Abd-Elshafi, *Electrochim. Acta*, 2006, **51**, 3269–3277.
40 R. W. Bosch, *Corrosion*, 2001, **57**, 60–70.
41 A. M. Eid, S. Shaaban and K. Shalabi, *J. Mol. Liq.*, 2020, **298**, 111980.
42 H. M. A. El-Lateef, Z. A. Abdallah and M. S. M. Ahmed, *J. Mol. Liq.*, 2019, **296**, 111800.
43 G. Gao and C. Liang, *Electrochim. Acta*, 2007, **52**, 4554–4559.
44 H. M. Abd El-Lateef, K. Shalabi and A. A. Abdelhamid, *J. Mol. Liq.*, 2021, **334**, 116081.
45 O. A. El-Gammal, *Inorg. Chim. Acta.*, 2015, **435**, 73–81.
46 O. A. El-Gammal, I. M. Abd Al-Gader and A. A. El-Asmy, *Spectrochim. Acta Mol. Biomol. Spectrosc.*, 2014, **128**, 759–772.
47 O. A. El-Gammal, *Spectrochim. Acta Mol. Biomol. Spectrosc.*, 2010, **75**, 533–542.
48 O. A. El-Gammal, *Spectrochim. Acta Mol. Biomol. Spectrosc.*, 2010, **75**, 533–542.
49 M. H. M. Hussein, M. F. El-Hady, H. A. H. Shehata, M. A. Hegazy and H. H. H. Hefni, *J. Surfactants Deterg.*, 2013, **16**, 233–242.
50 Y. M. Abdallah and H. Elzanaty, *Mater. Chem. Phys.*, 2019, **238**, 121925.
51 A. Singh, K. R. Ansari, M. A. Quraishi and S. Kaya, *J. Mol. Struct.*, 2020, **1206**, 127685.
52 M. Tourabi, K. Nohair, M. Traisnel, C. Jama and F. Bentiss, *Corros. Sci.*, 2013, **75**, 123–133.
53 A. S. Fouda, G. Y. Elewady, K. Shalabi and H. K. Abd El-Aziz, *RSC Adv.*, 2015, **5**, 36957–36968.
54 K. Shalabi, E. Abdel-Galil, A. H. El-Askalany and Y. M. Abdallah, *J. Mol. Liq.*, 2022, **348**, 118420.
55 K. F. Khaled, *Electrochim. Acta*, 2003, **48**, 2493–2503.
56 Y. M. Abdallah and K. Shalabi, *Prot. Met. Phys. Chem. Surf.*, 2015, **51**, 275–284.
57 H. Boudellioua, Y. Hamlaoui, L. Tifouti and F. Pedraza, *Appl. Surf. Sci.*, 2019, **473**, 449–460.
58 W. J. Lorenz and F. Mansfeld, *Electrochim. Acta*, 1986, **31**, 467–476.
59 Y. Yu, D. Yang, D. Zhang, Y. Wang and L. Gao, *Appl. Surf. Sci.*, 2017, **392**, 768–776.
60 M. A. Migahed, A. elgendy, M. M. EL-Rabiei, H. Nady and E. G. Zaki, *J. Mol. Struct.*, 2018, **1159**, 10–22.
61 D. D. Macdonald and M. C. H. McKubre, *Mod. Aspect. Electrochem.*, 1982, 61–150.
62 F. Mansfeld, *Corrosion*, 1981, **37**, 301–307.
63 K. Shalabi, O. A. El-Gammal and Y. M. Abdallah, *Colloids Surf. A Physicochem. Eng. Asp.*, 2021, **609**, 125653.
64 J. Haque, V. Srivastava, D. S. Chauhan, M. A. Quraishi, A. Madhan Kumar and H. Lgaz, *Sustain. Chem. Pharm.*, 2020, **16**, 100260.
65 S. A. Umoren, M. M. Solomon, U. M. Eduok, I. B. Obot and A. U. Israel, *J. Environ. Chem. Eng.*, 2014, **2**, 1048–1060.
66 M. M. Saleh, M. G. Mahmoud and H. M. Abd El-Lateef, *Corros. Sci.*, 2019, **154**, 70–79.
67 S. F. Mertens, C. Xhoffer, B. C. De Cooman and E. Temmerman, *Corrosion*, 1997, **53**, 381–388.
68 E. McCafferty and N. Hackerman, *J. Electrochem. Soc.*, 1972, **119**, 146.
69 E. Kuş and F. Mansfeld, *Corros. Sci.*, 2006, **48**, 965–979.
70 F. M. Reis, H. G. de Melo and I. Costa, *Electrochim. Acta*, 2006, **51**, 1780–1788.
71 M. Lagrenée, B. Mernari, M. Bouanis, M. Traisnel and F. Bentiss, *Corros. Sci.*, 2002, **44**, 573–588.
72 G. Trabanelli, C. Monticelli, V. Grassi and A. Frignani, *Cem. Concr. Res.*, 2005, **35**, 1804–1813.
73 K. Shalabi, A. M. Helmy, A. H. El-Askalany and M. M. Shahba, *J. Mol. Liq.*, 2019, **293**, 111480.
74 A. S. Fouda, K. Shalabi and A. A. Idress, *Green Chem. Lett. Rev.*, 2015, **8**, 17–29.
75 H. Ouici, M. Tourabi, O. Benali, C. Selles, C. Jama, A. Zarrouk and F. Bentiss, *J. Electroanal. Chem.*, 2017, **803**, 125–134.
76 G. Fan, H. Liu, B. Fan, Y. Ma, H. Hao and B. Yang, *J. Mol. Liq.*, 2020, **311**, 113302.
77 M. Bouanis, M. Tourabi, A. Nyassi, A. Zarrouk, C. Jama and F. Bentiss, *Appl. Surf. Sci.*, 2016, **389**, 952–966.
78 M. M. Solomon, S. A. Umoren, M. A. Quraishi and M. Salman, *J. Colloid Interface Sci.*, 2019, **551**, 47–60.
79 N. Z. N. Hashim, E. H. Anouar, K. Kassim, H. M. Zaki, A. I. Alharthi and Z. Embong, *Appl. Surf. Sci.*, 2019, **476**, 861–877.
80 P. Bommersbach, C. Alemany-Dumont, J. P. Millet and B. Normand, *Electrochim. Acta*, 2005, **51**, 1076–1084.
81 W. Temesghen and P. Sherwood, *Anal. Bioanal. Chem.*, 2002, **373**, 601–608.
82 A. Zarrouk, B. Hammouti, T. Lakhlifi, M. Traisnel, H. Vezin and F. Bentiss, *Corros. Sci.*, 2015, **90**, 572–584.
83 P. Mourya, P. Singh, R. B. Rastogi and M. M. Singh, *Appl. Surf. Sci.*, 2016, **380**, 141–150.
84 Y. Kharbach, F. Z. Qachchachi, A. Haoudi, M. Tourabi, A. Zarrouk, C. Jama, L. O. Olasunkanmi, E. E. Ebenso and F. Bentiss, *J. Mol. Liq.*, 2017, **246**, 302–316.
85 M. Zhao, Y. Cao, X. Liu, J. Deng, D. Li and H. Gu, *Nanoscale Res. Lett.*, 2014, **9**, 142.
86 T. G. A. A. Harris, R. Götz, P. Wrzolek, V. Davis, C. E. Knapp, K. Ly, P. Hildebrandt, M. Schwalbe, I. Weidinger, I. Zebger and A. Fischer, *J. Mater. Chem. A*, 2018, **6**, 15200–15212.
87 I. Moeez, H. D. Lim, J. H. Park, H. G. Jung and K. Y. Chung, *ACS Energy Lett.*, 2019, **4**, 2060–2068.
88 H. M. Abd El-Lateef, K. Shalabi and A. H. Tantawy, *New J. Chem.*, 2020, **44**, 17791–17814.
89 Y. Ma, F. Han, Z. Li and C. Xia, *ACS Sustain. Chem. Eng.*, 2016, **4**, 5046–5052.

90 N. Palaniappan, I. S. Cole and A. E. Kuznetsov, *RSC Adv.*, 2020, **10**, 11426–11434.
91 Y. Sasikumar, A. S. Adekunle, L. O. Olasunkanmi, I. Bahadur, R. Baskar, M. M. Kabanda, I. B. Obot and E. E. Ebenso, *J. Mol. Liq.*, 2015, **211**, 105–118.
92 I. Lukovits, E. Kálmán and F. Zucchi, *Corrosion*, 2001, **57**, 3–8.
93 H. M. Abd El-Lateef, S. Shaaban, M. M. Khalaf, A. Toghan and K. Shalabi, *Colloids Surf. A Physicochem. Eng. Asp.*, 2021, **625**, 126894.
94 A. K. Oyebamiji and B. B. Adeleke, *Int. J. Corros. Scale Inhib.*, 2018, **7**, 498–508.
95 Y. S. Mary, C. Y. Panicker, M. Sapnakumari, B. Narayana, B. K. Sarojini, A. A. Al-Saadi, C. Van Alsenoy and J. A. War, *Spectrochim. Acta Mol. Biomol. Spectrosc.*, 2015, **136**, 483–493.
96 L. H. Madkour, S. Kaya and I. B. Obot, *J. Mol. Liq.*, 2018, **260**, 351–374.
97 R. Hasanov, S. Bilge, S. Bilgiç, G. Gece and Z. Kiliç, *Corros. Sci.*, 2010, **52**, 984–990.
98 E. E. El-Katori, M. I. Nessim, M. A. Deyab and K. Shalabi, *J. Mol. Liq.*, 2021, **337**, 116467.
99 M. Özcan, I. Dehri and M. Erbil, *Appl. Surf. Sci.*, 2004, **236**, 155–164.
100 A. Dehghani, A. H. Mostafatabar, G. Bahlakeh and B. Ramezanzadeh, *J. Mol. Liq.*, 2020, 113914.
101 A. S. El-Tabei and M. A. Hegazy, *Chem. Eng. Commun.*, 2015, **202**, 851–863.
102 S. R. Gupta, P. Mourya, M. M. Singh and V. P. Singh, *J. Organomet. Chem.*, 2014, **767**, 136–143.
103 N. M. El Basiony, E. E. Badr, S. A. Baker and A. S. El-Tabei, *Appl. Surf. Sci.*, 2021, **539**, 148246.
104 Z. R. Farag, M. E. Moustapha, E. H. Anouar and G. M. Abd El-Hafeez, *J. Mater. Res. Technol.*, 2022, **16**, 1422–1434.